



Seasonality of eddy kinetic energy in an eddy permitting global climate model

Takaya Uchida ^{a,*}, Ryan Abernathey ^{a,b}, Shafer Smith ^c

^a Department of Earth and Environmental Sciences, Columbia University in the City of New York, USA

^b Division of Ocean and Climate Physics, Lamont-Doherty Earth Observatory, USA

^c Center for Atmosphere Ocean Science, Courant Institute of Mathematical Sciences, New York University, USA



ARTICLE INFO

Article history:

Received 8 February 2017

Revised 25 July 2017

Accepted 14 August 2017

Available online 14 August 2017

Keywords:

Mesoscale turbulence

Seasonality

Wavenumber spectra

Baroclinic instability

Linear stability analysis

ABSTRACT

We examine the seasonal cycle of upper-ocean mesoscale turbulence in a high resolution CESM climate simulation. The ocean model component (POP) has 0.1° resolution, mesoscale resolving at low and middle latitudes. Seasonally and regionally resolved wavenumber power spectra are calculated for sea-surface eddy kinetic energy (EKE). Although the interpretation of the spectral slopes in terms of turbulence theory is complicated by the strong presence of dissipation and the narrow inertial range, the EKE spectra consistently show higher power at small scales during winter throughout the ocean. Potential hypotheses for this seasonality are investigated. Diagnostics of baroclinic energy conversion rates and evidence from linear quasigeostrophic stability analysis indicate that seasonally varying mixed-layer instability is responsible for the seasonality in EKE. The ability of this climate model, which is not considered submesoscale resolving, to produce mixed layer instability although damped by dissipation, demonstrates the ubiquity and robustness of this process for modulating upper ocean EKE.

© 2017 Elsevier Ltd. All rights reserved.

1. Introduction

Mesoscale turbulence is ubiquitous in the ocean and has significant impacts on the large-scale ocean circulation and its interaction with the climate (e.g. Jayne and Marotzke, 2002; Volkov et al., 2008; Lévy et al., 2010; Griffies et al., 2015). Ocean currents are most energetic in the mesoscale range, on the order of tens to a few hundred kilometers. Mesoscale turbulence is driven by baroclinic instability of the main thermocline (Gill et al., 1974; Smith, 2007), and is relatively well described by quasi-geostrophic (QG) models (Rhines, 1979; Held et al., 1995), in which enstrophy and energy conservation lead to the inverse cascade of energy from small to large scales (Charney, 1971). Below the mesoscale lies the submesoscale, which feeds off of the available potential energy (APE) in the mesoscale fronts, particularly in the mixed layer (Boccaletti et al., 2007).

A number of recent observational and modeling papers have demonstrated a pronounced seasonality in surface EKE in the submesoscale range, roughly 10–100 km (Mensa et al., 2013; Qiu et al., 2014; Sasaki et al., 2014; Callies et al., 2015; Brannigan et al.,

2015; Rocha et al., 2016b; Buckingham et al., 2016). Most of the studies cited are regional or from idealized models, thus global patterns have not yet been established. Moreover, there are at least four main hypotheses proposed to explain this seasonality: (i) variation in internal gravity wave energy due to seasonality in upper ocean stratification (Rocha et al., 2016b); (ii) variation in frontogenesis (FG) due to seasonality in lateral strain and convergence in horizontal density gradients (Mensa et al., 2013); (iii) variation in the interior baroclinic instability (BCI) due to seasonality in the vertical shear of the full-depth background state (Qiu et al., 2014); and (iv) variation in the mixed-layer (ML) BCI due to seasonality in ML stratification, depth and vertical shear in the mixed layer (Boccaletti et al., 2007; Qiu et al., 2014; Callies et al., 2016). There is as yet no strong consensus about the relative roles of these mechanisms on a global scale.

Current generation satellite altimetry products provide global observations of sea surface height (SSH), and thus geostrophic velocity, but the spread of the tracks and instrument noise limit the effective resolution to about 100 km (Xu and Fu, 2012), which is just sufficient to see the peak of the mesoscale. The almost-submesoscale-resolving Surface Water Ocean Topography (SWOT) satellite (Fu and Ferrari, 2008) is expected to launch in 2021, and until then, investigations of submesoscale and submesoscale-driven seasonality in EKE must rely on models.

* Corresponding author at: 205A Oceanography 61 Route 9W - PO Box 1000 Palisades, NY 10664-8000, USA

E-mail address: takaya@deo.columbia.edu (T. Uchida).

In this paper, we investigate seasonal variability of eddy kinetic energy (EKE) in a state-of-the-art global climate model; specifically the 0.1° -resolution configuration of the Parallel Ocean Program (POP) model, run within the fully-coupled Community Earth System Model (CESM) simulation described in Small et al. (2014). To our knowledge, the seasonality of ocean turbulence has not been examined in a coupled model on a global scale. According to the criteria of Hallberg (2013), this configuration ranges from mesoscale-resolving at low latitudes to mesoscale-permitting at high latitudes. Although this is very fine resolution for a climate model — finer than resolved by current generation altimeters — it is coarse compared to recent numerical studies of submesoscale seasonality, some of which have used a spatial resolution of 1 km or even higher (Mensa et al., 2013; Sasaki et al., 2014; Gula et al., 2014; Brannigan et al., 2015; Rocha et al., 2016a; 2016b). The lack of resolution is a necessary trade-off for a global analysis. Moreover, analysis of such a model should provide a useful test bed for future work on SWOT observations.

Driven by this connection to altimetric observations, we focus on the analysis of surface fields, especially on wavenumber power spectra, which provide a practical way to characterize scale-dependent variance and have been widely used in related studies (e.g. Stammer, 1997; Thomas et al., 2008; Capet et al., 2008b; Xu and Fu, 2011; 2012). An oft-cited motivation for spectral analysis is its connection to inertial-range turbulence theories, which provide specific predictions for spectral power law scalings that vary with the nature of the turbulence, suggesting a tempting way to test ideas. For example, Xu and Fu (2012) made a global estimate of two-dimensional (2D) along-track spectral slopes of SSH observed by satellite altimeters on *Jason-1* and *Jason-2*. They found that in regions of high eddy activity, the SSH spectral slopes had values between k^{-5} and $k^{-11/3}$, which are consistent with predictions by QG (Charney, 1971) and surface-QG (SQG) theory (Blumen, 1978; Held et al., 1995; Lapeyre and Klein, 2006), respectively. However, such theories formally only apply to scales that are neither directly forced nor dissipated, are stationary in time, and reflect only one underlying dynamics. Callies et al. (2016) points out that the submesoscale range is likely directly forced, violating the inertial assumption, and Dufau et al. (2016) argues that previous estimates of spectral slopes from altimetry which do not properly account for the spatial and temporal variability of significant wave height (e.g. Xu and Fu, 2012) may be contaminated by observational noise even in the mesoscale range. Moreover, the very temporal variability we seek to study implies temporal non-stationarity. Consequently, our study does not emphasize specific values of the spectral slopes; rather, we simply use spectra as one of many tools to characterize energy variations in a scale-dependent way.

Despite the limitations imposed by the model resolution and strong damping due to dissipation, we show that the POP simulation resolves some submesoscale generated energy cascading up to the mesoscale. Moreover, many lines of evidence — including linear stability analysis, predictions for energy transfer rates, and phase correlations — point to an inverse cascade of submesoscale energy generation by mixed-layer instability as the primary driver of this seasonality.

The paper is organized as follows. In Section 2, we give a brief description of the POP model. The results of spectral analysis and comparison of the spectral slopes among seasons are shown in Section 3. In Section 4 we discuss baroclinic instability at the mesoscale and submesoscale, and detail our evidence for MLI as a main source of seasonality in EKE. In Section 5, we examine two other possible drivers of seasonality in small-scale EKE: intertia-gravity waves and frontogenesis. We summarize and conclude in Section 6. The details of our spectral analysis and linear stability analysis are given in the appendix.

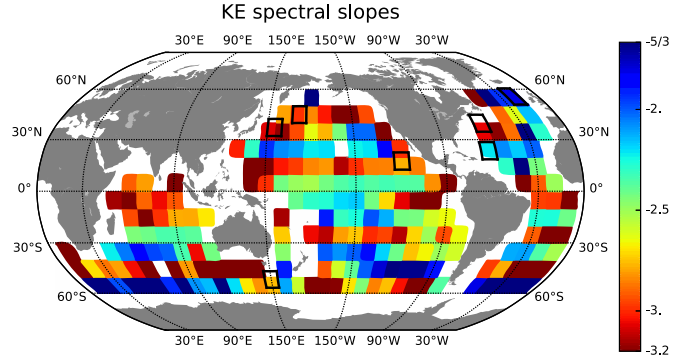


Fig. 1. Annual mean of spectral slopes at scales above $200\text{--}250$ km ($4 \times 10^{-3} \text{--} 5 \times 10^{-3}$ cpkm). The black boxes indicate the seven regions (Kuroshio, north of Kuroshio, east Pacific, Gulf Stream, Sargasso Sea, northeast Atlantic and the ACC) we consider in detail.

2. Description of the numerical model

The ocean simulation we examine is a part of the fully-coupled global simulation using the CESM described in Small et al. (2014), which was run under present-day greenhouse gas conditions for 100 years, similar to McClean et al. (2011). The POP model, which is the ocean component, is a level-coordinate ocean general circulation model that solves the three-dimensional primitive equations for ocean dynamics. The hydrostatic and Boussinesq approximations are prescribed, and the model employs a B-grid (scalars at cell centers, vectors at cell corners) for the horizontal discretization scheme. The time discretization scheme uses a three-time-level second-order-accurate modified leap-frog scheme for stepping forward in time. The diffusive terms are evaluated using a forward step.

Subgrid scale horizontal mixing is parameterized using bi-harmonic diffusivity and viscosity, with the coefficients spatially varying with the equatorial values of $A_H = -3.0 \times 10^9 \text{ m}^4/\text{s}$ and $A_M = -2.7 \times 10^{10} \text{ m}^4/\text{s}$ respectively. The vertical diffusion depends on the K-profile parameterization (KPP) of Large et al. (1994). Further details about the discretization and advection schemes of the primitive equations and parameterization methods are described in the Parallel Ocean Program Reference Manual (Smith et al., 2010). The horizontal grid spacing in the POP simulation is approximately 0.1° in latitude/longitude. Each component of the coupled model exchanges information at different time intervals, with the atmosphere, sea ice, and land models coupling every time step (15 min), and the ocean every 6 h. The simulation outputs at the ocean surface were saved as daily averages, while interior information was saved as monthly averages. The available model output constrains the scope of our analysis; since the monthly averaging filters out lots of small-scale variance, we focus our spectral analysis at the surface. More details of the model setup can be found in Small et al. (2014).

A video of the sea surface temperature in the Kuroshio region is available online at <https://vimeo.com/channels/oceanodynamics/99933667>. This video clearly shows the formation of secondary instabilities on the fronts of mesoscale eddies; this process appears to be much more active in winter, when mixed layers are deep. Although the spatial resolution of this model (0.1°) is not considered submesoscale resolving, the video suggests that some submesoscale processes are captured by the model. This visualization provided the motivation for our subsequent quantitative analysis of seasonality.

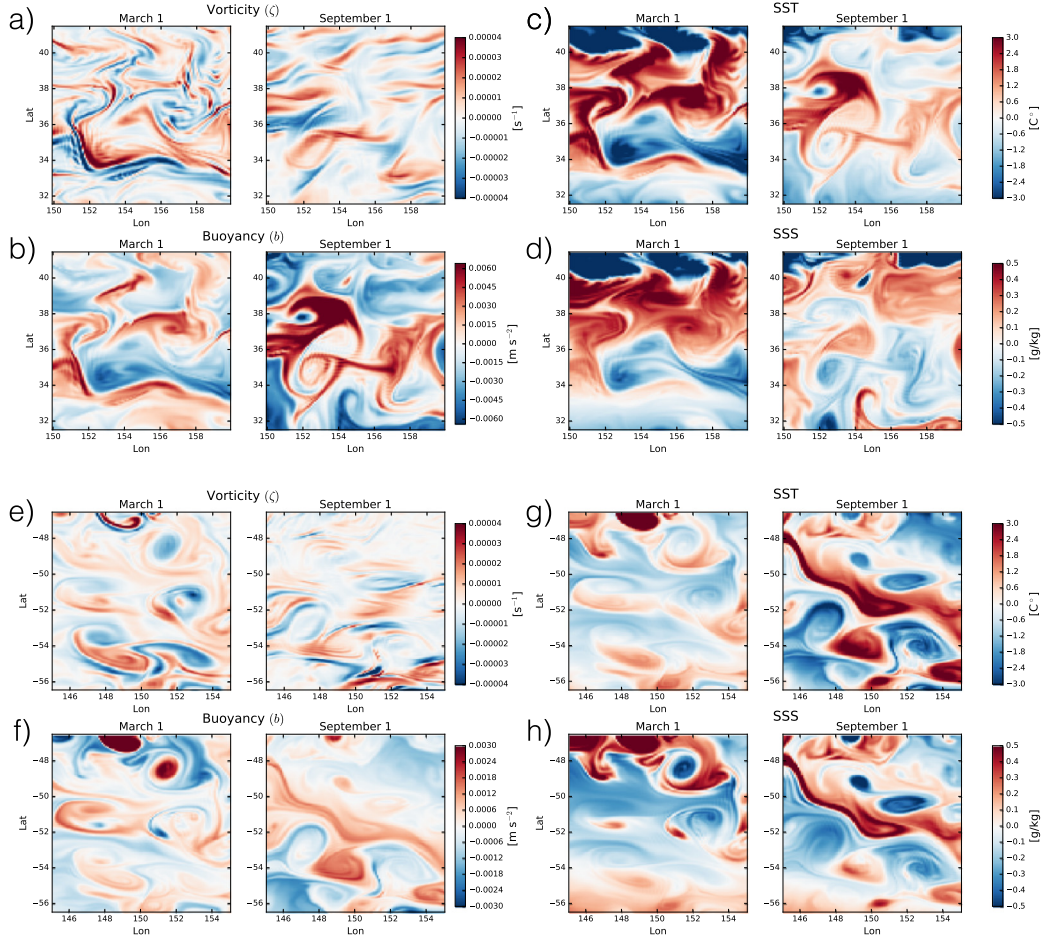


Fig. 2. Snapshot of the anomaly fields of vorticity (ζ), buoyancy (b), SST and SSS on March 1, and September 1. The upper panels (a, b, c and d) correspond to the Kuroshio region (lon: 150.0–160.0E, lat: 31.5–41.5N) and the lower panels (e, f, g and h) to the ACC region (lon: 145.0–155.0E, lat: 56.5–46.5S).

3. Spectral analysis of the velocity and tracer fields

Spectral analysis provides a practical way to characterize the scale-dependent variance in the simulation. To resolve regional variability, we split up the domain over the globe into 10° latitude-longitude boxes and calculate the spectra for each subdomain. For every daily-averaged field in each subdomain, we remove the spatial mean by subtracting the bi-linear trend derived from the least-square plane fit of the horizontal fields and apply a 2D Hanning window. In deriving the wavenumber spectrum, we approximate a local tangent plane in Cartesian geometry and take the 2D Fourier transform of the anomaly fields. We then take the average over the azimuthal direction to create an isotropic spectrum. We sample the spatial fields every 13 days, which is approximately the temporal decorrelation time. For the purposes of calculating the error, each individual spectrum is therefore treated as an independent realization of the process. Using 41 years of data, we have 1135 individual spectra. Numerical implementation and normalization of the spectra is discussed in the Appendix A.3.

3.1. Snapshots of tracer fields and example of spectra

The annual mean spectral slopes are shown in Fig. 1 (see Section 3.2 for description of how slopes are fit). In most regions, the spectral slopes are in the range predicted by QG theory but some regions have slopes steeper than -3 , which is likely due to the presence of dissipation. Before examining the seasonal variability of this global map, we first examine the details of the spa-

tial and spectral fields in a few energetic regions of the ocean (Kuroshio, Gulf Stream, and ACC). The location of the regions is shown in Fig. 1. (Additional regions are presented in Appendix A.1)

Fig. 2 shows instantaneous spatially detrended fields of relative vorticity (ζ) and buoyancy ($b = -g\delta\rho/\rho_0$; $\delta\rho = \rho - \rho_0$, $\rho_0 \equiv 1025 \text{ kg/m}^3$) on March 1, and September 1, (representative of winter and summer in the northern hemisphere and vice versa in the southern hemisphere) in model year 46. We see the spatial fields have more small scale features and sharper fronts on March 1, in the Kuroshio region and September 1, in the ACC region, particularly in the vorticity field.

Fig. 3(a-c) shows the seasonally-averaged isotropic wavenumber spectra of EKE for the Kuroshio, Gulf Stream and ACC regions.

Boreal winter is defined as January, February and March (JFM), spring as April, May and June (AMJ), summer as July, August and September (JAS) and autumn as October, November and December (OND). (The spectra for the other four regions are shown in Appendix A.1.) Comparing the EKE spectra for each season, the spring spectra have the highest energy in the lower mesoscale range (between 50 km and 100 km, i.e. 10^{-2} – 2×10^{-2} cpkm) while autumn has the lowest energy. At the smallest scales, the EKE spectra have most power in winter and least power in summer. (Buoyancy spectra are presented and discussed in Section 3.3.)

3.2. Seasonal variations kinetic energy spectra

Theoretical models of ocean mesoscale turbulence predict spectral slopes in the inertial range (Charney, 1971; Held et al., 1995)

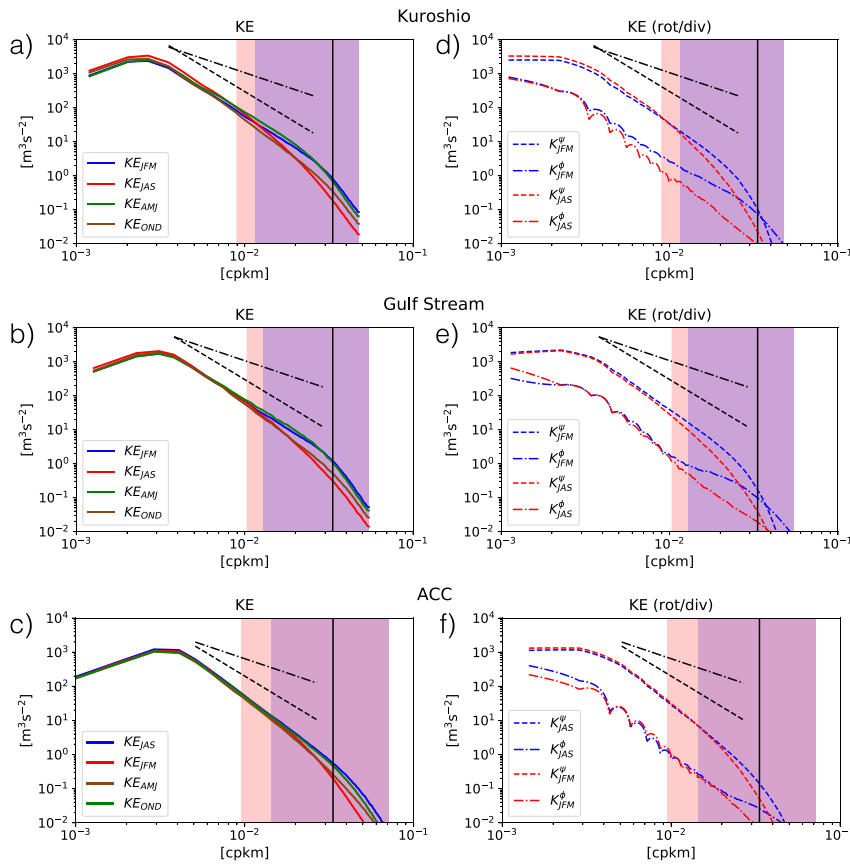


Fig. 3. Seasonally-averaged EKE spectra in eddy active regions: (a) Kuroshio, (b) Gulf Stream, and (c) ACC in Fig. 1. The shading shows the dissipation range defined as where 80% of the dissipation due to biharmonic diffusion occurs (blue: winter, red: summer). The black dashed and dotted lines show the spectral slope of -3 and $-5/3$ respectively. The black vertical line indicates the 30 km scale. The dashed and dotted spectra in panels (d), (e) and (f) show the rotational and divergent component of EKE respectively for each of these regions. The 95% confidence intervals were thinner than the lines used to plot the spectra and so are not shown. (For interpretation of the references to color in this figure legend, the reader is referred to the web version of this article.)

and many previous studies have used spectral slopes to characterize ocean turbulence in observations and numerical models (e.g. Stammer, 1997; Capet et al., 2008b; Xu and Fu, 2011; 2012). As pointed out by Callies et al. (2016), however, the actual values of spectral slopes are not dynamically unique and inertial range theories are invalid at scales that are directly forced. Furthermore, given the strong role of dissipation and the relatively small wavenumber range resolved by our model, it is unlikely that inertial range theories apply quantitatively to this simulation. Consequently, we focus on the seasonal *changes* in slopes, rather than their absolute values. These slope changes indicate a seasonally varying partition of energy between large and small scales. The slopes were calculated by fitting a straight line to the log-log spectrum using the least-square method. Due to limited spatial resolution and the influence of sub-grid dissipation, the slope fit is very sensitive to the choice of wavenumber range. In addition to dissipating EKE at each scale, the numerical dissipation also removes EKE due to baroclinic instability that would have otherwise cascaded upscale, so the spectral slopes are expected to be steeper than predicted by QG turbulence theories.

We address dissipation by explicitly calculating the momentum tendency due to lateral biharmonic viscosity in the spectral domain (see Appendix A.4 for details). We define the “dissipation range” as the wavenumber range above which 80% of dissipation occurs. From Fig. 3, we see that the dissipation range is broad and extends up to 100 km. This is likely the main cause for the relatively steeper spectral slopes at high wavenumbers. The influence of dissipation means it is problematic to compare the actual values

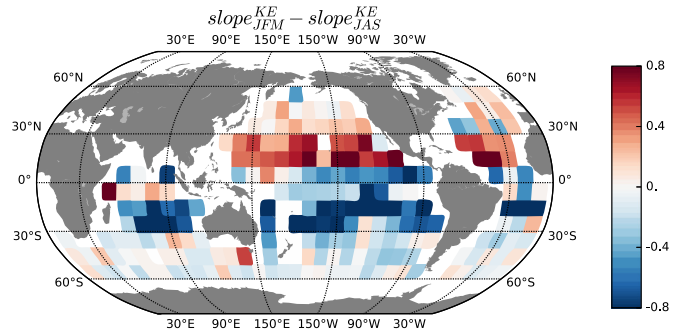


Fig. 4. Difference of spectral slopes of EKE between JFM and JAS at scales between 200 km and 250 km (i.e. $4 \times 10^{-3} - 5 \times 10^{-3}$ cpkm).

of slopes in this range and possibly below with turbulent inertial range theory. The dissipation is broad-band so the inertial range is very narrow, if it exists at all. The seasonal variability could also violate the stationarity requirement for such a range to exist. The slope fit is, therefore, performed on scales between 200 km and 250 km (i.e. $4 \times 10^{-3} - 5 \times 10^{-3}$ cpkm), which is outside of the dissipation range globally. Fig. 4 shows the resulting slope difference between winter (JFM) and summer (JAS), which is consistent with the regional spectra (Fig. 3).

The slope analysis neglects the broad dissipation range, but the strongest variations in spectral energy occur within the dissipation

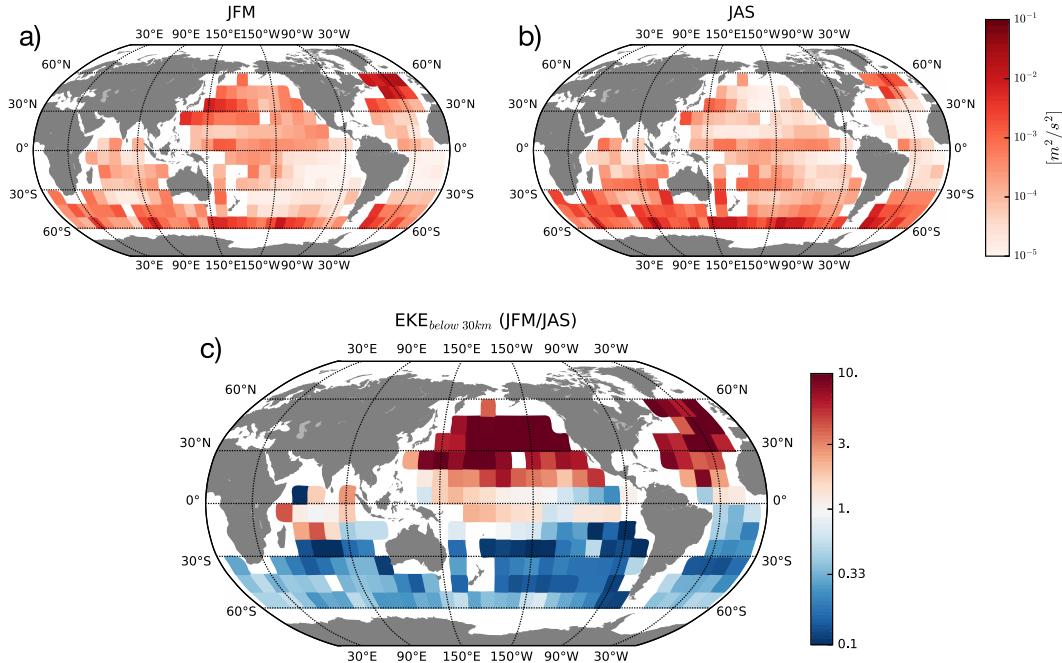


Fig. 5. Seasonal climatology of EKE at scales smaller than 30 km (3.3×10^{-2} cpm) for JFM (a), JAS (b) and the ratio between the two (EKE_{JFM}/EKE_{JAS}) (c).

range. To quantify the energy at the smallest scales, we perform a high pass in the spectral range representing scales below 30 km (3.3×10^{-2} cpm); the resulting seasonal difference in small scale EKE is shown in Fig. 5. A strong seasonal cycle is clearly present in both hemispheres. As visible in Fig. 3 these results are not sensitive to the specific wavenumber range.

Seasonality in submesoscale turbulence has been noted in numerous very-high-resolution regional simulations (Mensa et al., 2013; Sasaki et al., 2014; Qiu et al., 2014) but not in a global model with $1/10^\circ$ resolution. In order to estimate the relative validity of the amplitude of this model's seasonal cycle, we compare the POP model EKE levels with the values found by Sasaki et al. (2014) (Fig. 5 (a) in their paper¹). Sasaki et al. (2014) examined a regional model of the Kuroshio with the resolution of $1/30^\circ$ in the horizontal and 100 vertical levels, finding a strong seasonal cycle of submesoscale turbulence driven by mixed-layer instability (MLI). The domain they analyzed was $148^\circ\text{E}-168^\circ\text{W}, 20^\circ\text{N}-43^\circ\text{N}$; our closest regional $10^\circ \times 10^\circ$ box is $150^\circ\text{E}-160^\circ\text{E}, 31.5^\circ\text{N}-41.5^\circ\text{N}$. The annual-mean KE(k) at 10^{-2} cpm is approximately $120 \text{ m}^3/\text{s}^2$ in their model and $50 \text{ m}^3/\text{s}^2$ in ours. (It is not surprising that their spectrum has higher energy levels since their model has a higher spatial resolution.) Comparing the ratio of energy levels at the scale 3×10^{-2} cpm between winter and summer, the ratio is around 5 in theirs and 4 in ours. This comparison suggests that the POP simulation produces seasonal variability of comparable amplitude to submesoscale resolving models, despite the overall lower energy level.

3.3. Temperature, salinity, and buoyancy spectra

We also calculated seasonal isotropic power spectra for potential sea-surface temperature θ (SST), sea-surface salinity S (SSS), and sea-surface buoyancy b . The buoyancy is defined as $b = -g\delta\rho/\rho_0$ where $\delta\rho = \rho - \rho_0$ and ρ is derived using the gsw TEOS-10 package (McDougall and Barker, 2011) and $\rho_0 =$

1025 kg/m^3 . The tracer spectra for the three example regions are shown in Fig. 6. The spectral slope of buoyancy is generally shallower than that of KE, a finding consistent with results of Callies et al. (2016, c.f. Fig.10 in their paper), although the energy levels themselves are inconsistent with observed sub-surface buoyancy spectra (Callies et al., 2015). In contrast to EKE, we do not observe significant seasonal variations in the spectral slope for these tracers. This finding is consistent with the SST spectrum of Schloesser et al. (2016, c.f. Fig. 6 in their paper at scales larger than 10 km). There is, however, substantial seasonal variability in the overall power level across all length scales.

To examine the seasonality of tracer variance globally, Fig. 7 shows maps of the seasonal difference in small-scale power for buoyancy, SST and SSS between winter and summer. (Since the tracer power level varies uniformly across all analyzed wavenumbers, the choice of averaging band is unimportant here.) The SST power levels show hemispheric seasonality broadly similar to EKE: more SST variance in winter, less in summer. The SSS power levels, in contrast, do not have a coherent hemispheric-scale seasonality, with having opposite seasonality from EKE and SST in some regions. Due to the possibility of compensation between SST and SSS variability, buoyancy variance is not a linear combination of SST and SSS variance. The spatial pattern of seasonal variability of the buoyancy variance (Fig. 7a) more closely resembles the variability of SSS, even at low and mid latitudes. It is likely that a wide range of different processes, especially air-sea interaction, contribute to these patterns of seasonal variability (F. Bryan (2017) personal communication).

From the buoyancy field, it is tempting to compute surface available potential energy (APE), especially given its relevance to baroclinic instability (discussed in the next section). Studies of the energy cycle in global ocean models (e.g. Chen et al., 2016) commonly employ the approximation $\text{APE} \approx b^2/N^2$, appropriate in a well-stratified incompressible Boussinesq fluid (e.g. Vallis, 2006). We calculated this quantity in the model mixed layer using daily buoyancy variance b and a seasonal, 10° -box-averaged climatology of N^2 , but found that the APE level and its seasonality were completely dominated by the seasonal climatology of the buoyancy fre-

¹ Keeping in mind that the units in Sasaki et al. (2014) are $[\text{cm}^2\text{s}^{-2}(\text{cpkm})^{-1}]$, there is a factor of 20π when converting them to $[\text{m}^3/\text{s}^2]$

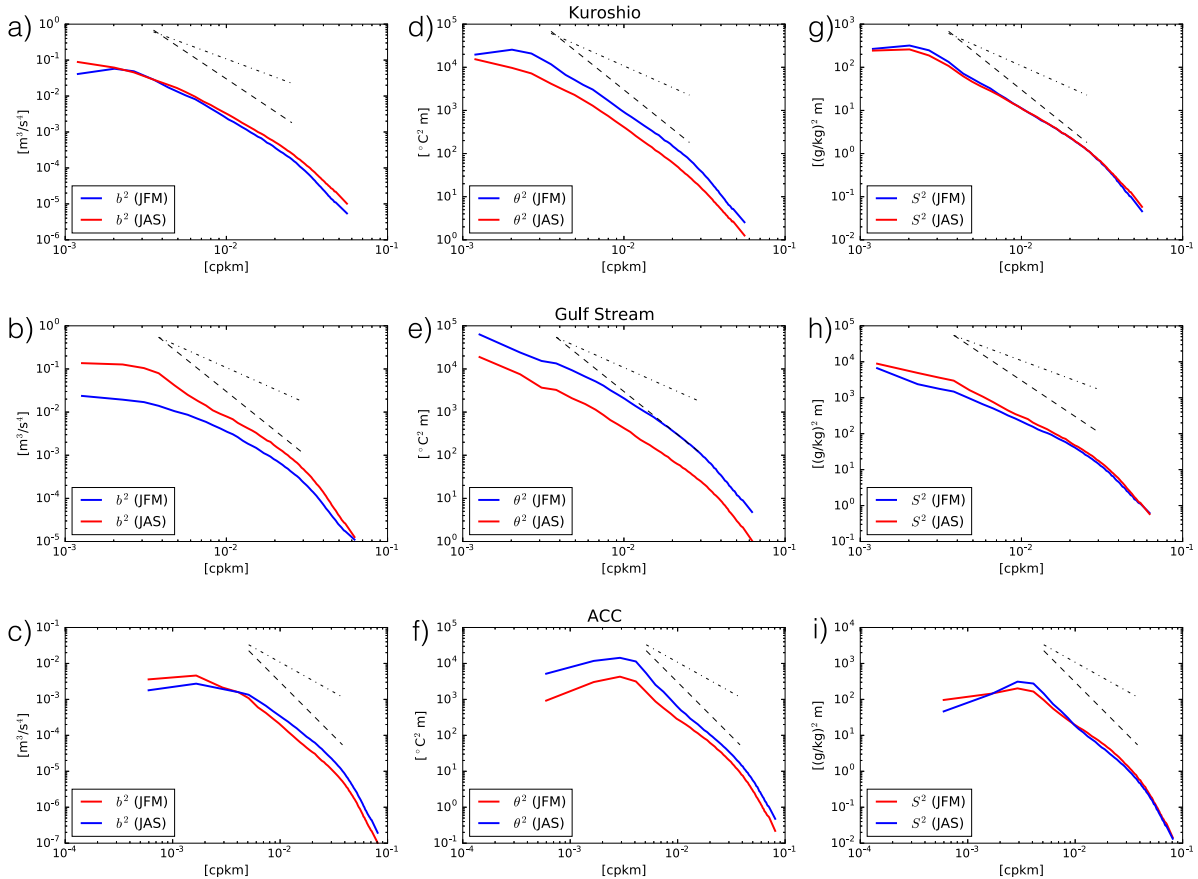


Fig. 6. Isotropic wavenumber spectra of buoyancy (a–c), SST (d–f) and SSS (g–i) in the Kuroshio, Gulf Stream and ACC domain in Fig. 1 (blue: winter, red: summer). The black dashed and dotted lines show the spectral slope of -3 and $-5/3$ respectively. (For interpretation of the references to color in this figure legend, the reader is referred to the web version of this article.)

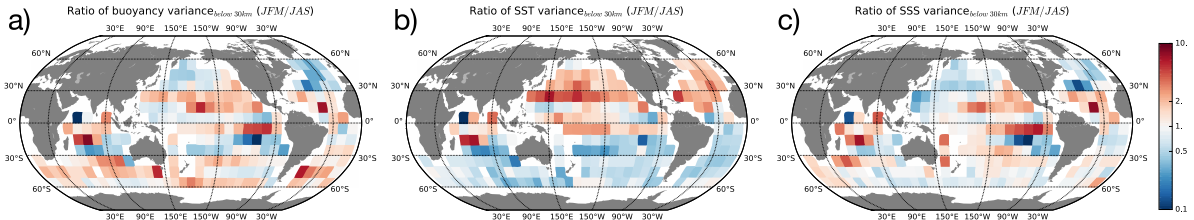


Fig. 7. Ratio of tracer variance between JFM and JAS at scales below 30 km (i.e. 3.3×10^{-3}) (a) buoyancy, (b) SST and (c) SSS).

quency (N^2), with almost no role for the buoyancy variance itself. Upon reflection, this is unsurprising: the APE approximation used is not suited for weakly-stratified boundary layers, and even less so in the artificial mixed layer of the POP model, which is set by the K-Profile Parametrization scheme (Large et al., 1994) and lacks representation of the submesoscale processes that act to restratify it in the real ocean.

4. Evidence for mixed-layer baroclinic instability as the source for seasonal variations in EKE

Baroclinic instability (BCI) converts available potential energy (APE) of the background ocean state into eddy kinetic energy (EKE), generally at or near the scale of the most linearly unstable mode (Gill et al., 1974). A leading hypothesis for the generation of seasonality in the submesoscale range is the mixed layer instability (MLI), a form of BCI which extracts potential energy from buoyancy fronts in the mixed layer (Boccaletti et al., 2007). Since mixed layer depth and stratification vary substantially over the seasonal cycle, EKE production from MLI has been shown to be much higher

in winter, when mixed layers are deep and stratification is weak (Callies et al., 2015; 2016). However, seasonal variations in deep BCI, which draws energy from the main thermocline, have also been implicated in driving seasonal variations in EKE in the North Equatorial Counter Current region (Qiu et al., 2014).

MLI occurs on scales near the ML deformation wavelength (L_d^{ML}), which ranges from several km to less than 1 km (Boccaletti et al., 2007). The study of MLI in numerical models has consequently mostly focused on models with grid spacing of roughly 4 km or less (e.g. Mensa et al., 2013; Sasaki et al., 2014; Qiu et al., 2014). The relatively coarse resolution of the POP simulation, and the large role of dissipation at small scales (as noted in the previous section), would presumably prevent MLI from emerging. Nevertheless, in this section we show evidence that the cause of the seasonal variability in EKE described above is indeed MLI.

4.1. Baroclinic conversion rate

BCI produces eddy kinetic energy from potential energy via the vertical eddy flux of buoyancy $w' b'$ (Vallis, 2006). When high-

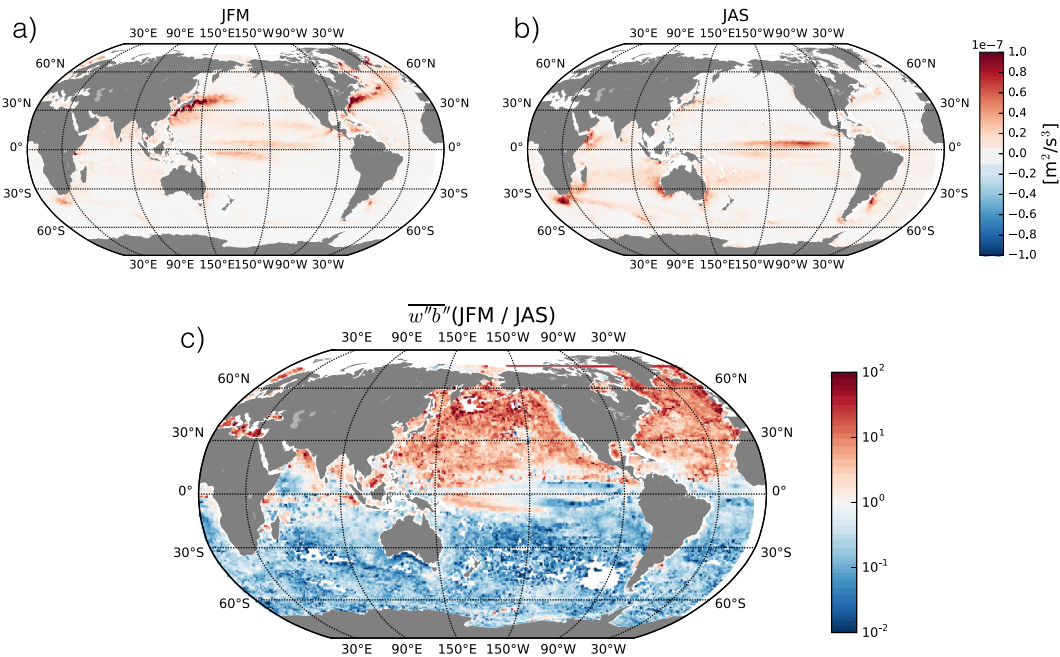


Fig. 8. Seasonal climatology of sub-monthly APE conversion rate ($\overline{w''b''}$) for JFM (a), JAS (b) and the ratio between the two (c).

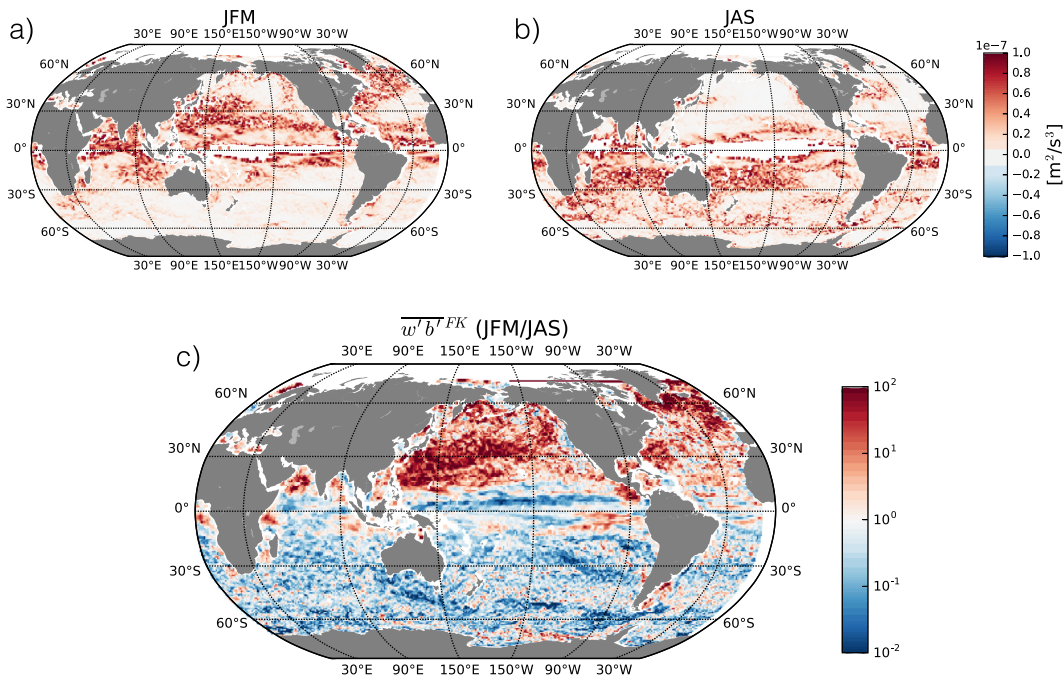


Fig. 9. APE conversion rate following the parametrization by Fox-Kemper et al. (2008) ($\overline{w''b'^{FK}}$) for JFM (a), JAS (b) and the ratio between the two (c). Values near the equator are masked out for (a) and (b) as the Coriolis parameter becomes small.

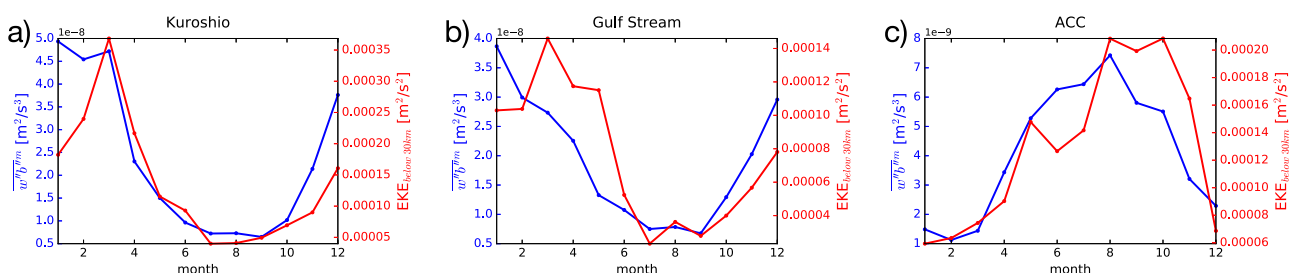


Fig. 10. Seasonal phase of $\overline{w''b''}$ and EKE in the Kuroshio (a), Gulf Stream (b) and ACC (c) domain in Fig. 1.

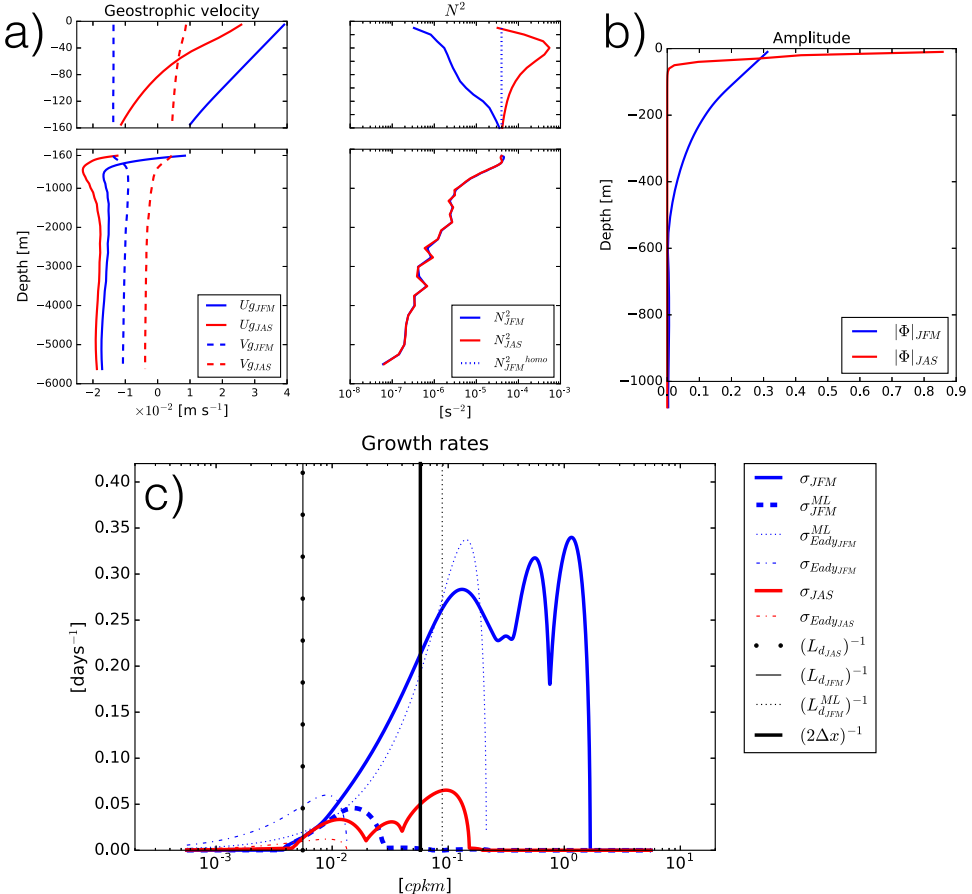


Fig. 11. Kuroshio region in Fig. 1 for (a) the geostrophic velocity and buoyancy frequency. We also show the homogenized buoyancy frequency in the ML for winter and summer. The figure is divided at the ML base. (b) Amplitude of the unstable mode with the largest growth rate closest to the Nyquist wavenumber. (c) Numerical solution of growth rates in the Kuroshio region for each season plotted against the zonal inverse wavelength with zero meridional wavenumber: linear instability solved with original profile (solid line) and with homogenized stratification in the ML (dashed line). The Eady (dot-dashed line) and ML Eady (dotted line) growth rate are shown as well. The zonal inverse wavelength was defined between the range of 10^{-1} to $10^3 L_d^{-1}$. The Rossby deformation inverse wavelength are shown in black thin lines and the thick black line indicates the Nyquist wavelength.

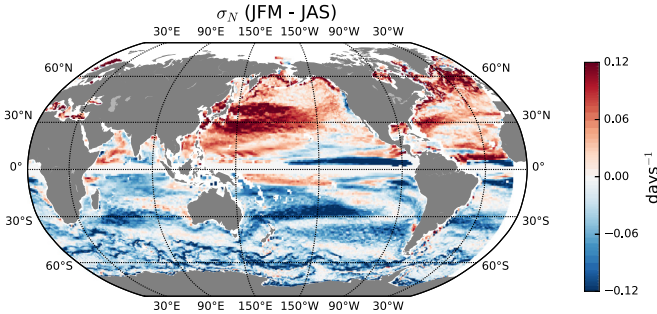


Fig. 12. Seasonal difference of the maximum growth rate solved numerically at the Nyquist wavelength.

frequency data is available, this term can be calculated in the spectral domain, i.e. as the cross spectrum $\Re\{\hat{w}^*\hat{b}\}(k)$, which reveals the spatial scales of energy production from BCI. This analysis has been used to demonstrate the link between the scales and growth rates of the most unstable normal modes identified by linear stability analysis and the finite-amplitude production of kinetic energy in fully developed, nonlinear baroclinic turbulence (e.g. Holland, 1978; Qiu et al., 2014). Callies et al. (2016) used such cross spectra to show the importance of MLI in energizing submesoscale turbulence in idealized QG simulations.

In analyzing baroclinic conversion from the POP model, we are somewhat constrained by the available output. High frequency (daily) data were only saved for the surface, precluding a spectral decomposition of w and b in the interior. Interior fields were saved as monthly averages, which heavily filters small-scale fluctuations. However, a six year portion of the integration was conducted in which this monthly-averaged interior data included the vertical tracer fluxes $\bar{w}\bar{\theta}^m$ and $\bar{w}\bar{S}^m$, where the m superscript indicates a temporal average over a single month. From this output, the monthly-averaged buoyancy flux can be calculated as $\bar{w}\bar{\theta}^m \approx g(\alpha\bar{w}\bar{\theta}^m - \beta\bar{w}\bar{S}^m)$ where α is the thermal expansion and β the haline contraction coefficient determined from the seasonal climatologies for each 1° grid box.

To isolate the baroclinic conversion associated with small-scale motions, we calculate the *sub-monthly* contribution to the vertical buoyancy flux. The sub-monthly fluctuations are defined as anomalies from the instantaneous monthly average (*not* the climatology) and denoted with a double prime: e.g. $u'' \equiv u - \bar{u}^m$. This temporal high-pass filter acts as a crude spatial high-pass filter. We tested the effect of this filtering on the surface horizontal velocity fields, for which daily data is available, and found that it strongly attenuates the EKE spectrum at wavenumbers less than 5×10^{-3} cpkm while leaving the smaller scales mostly unchanged. (See Appendix A.3 for discussion and figure.) This filtering thus allows us to focus on baroclinic conversion in the high wavenumber range where we observe the strongest seasonality in EKE.

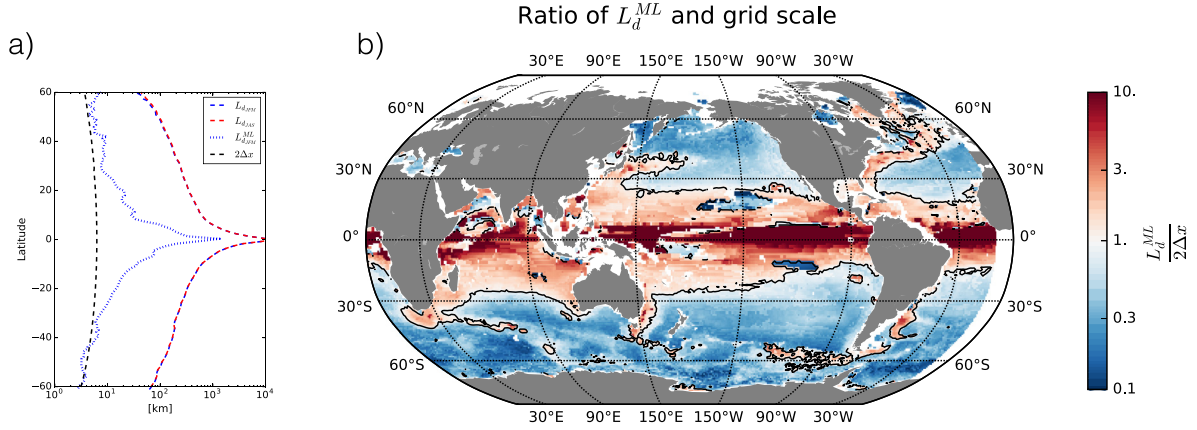


Fig. 13. (a) The zonal average of the Rossby radius (L_d) for winter and summer and the ML Rossby radius (L_d^{ML}) for winter between 60S and 60N 60N. The black dashed line indicates the Nyquist wavelength. (b) Ratio of the Rossby wavelength calculated over the mixing layer to the Nyquist wavelength ($L_d^{ML}(2\Delta x)^{-1}$). The values of L_d^{ML} used in the northern hemisphere are values during JFM (boreal winter) and JAS (austral winter) for the southern hemisphere. The black contours indicate where the ratio is unity.

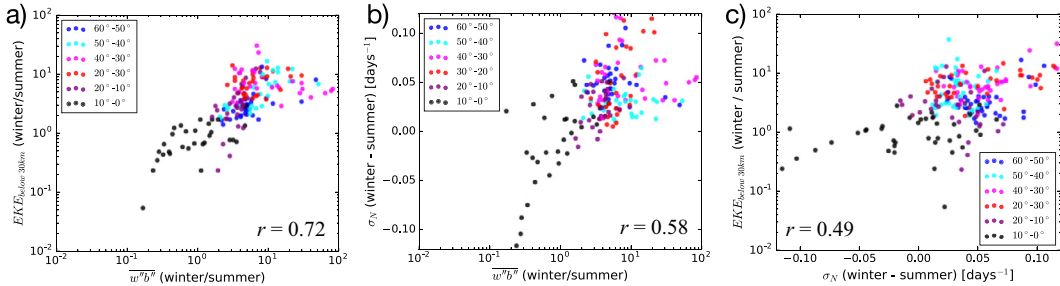


Fig. 14. Scatter plot of seasonal difference of (a) EKE against $w''b''$, (b) σ_N against $w''b''$ and (c) EKE against σ_N . Negative values of $w''b''$ were masked out before calculating the correlation. The colors represent each latitudinal band and the correlation coefficient (r) is calculated for the globe.

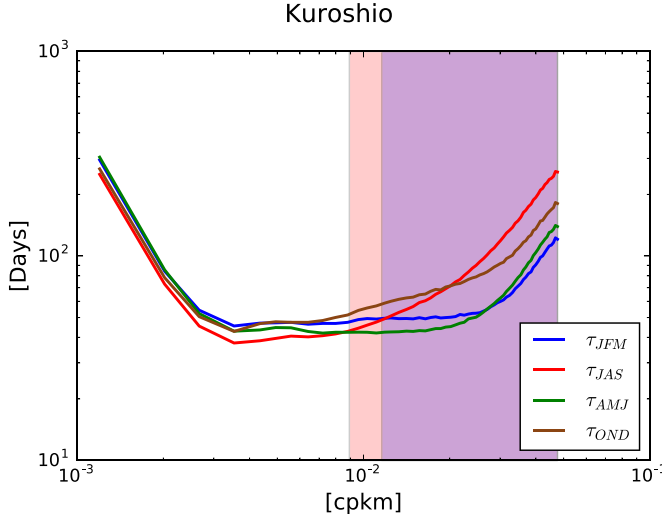


Fig. 15. Eddy turnover timescale in days for the Kuroshio region in Fig. 1. The color shadings represent the EKE dissipation range for JFM (blue) and JAS (red). (For interpretation of the references to color in this figure legend, the reader is referred to the web version of this article.)

Although we can't directly calculate w'' (or its spectrum) from the available interior output, we can calculate the sub-monthly vertical buoyancy flux as

$$\overline{w''b''}^m = \overline{wb}^m - \overline{w}^m \overline{b}^m. \quad (1)$$

We do this for each month of the six years in which this output is available. The seasonal climatology of $\overline{w''b''}$ (superscript m dropped because we are dealing with a climatology) is then calculated by grouping together all the months from each season and averaging

over the upper 100 m of the water column. (Results are not highly sensitive to averaging depth.)

The results of this analysis for JFM and JAS are shown in Fig. 8, together with the seasonal difference. The climatologies show that $w''b''$ is positive nearly everywhere, indicating conversion of potential energy to kinetic energy, as expected in MLI and BCI in general. The conversion is strongest in energetic regions such as the Gulf Stream, Kuroshio, Agulhas, ACC, and Leeuwin current. The strong seasonal cycle is readily visible by comparing the two seasons and emerges clearly in the difference plot. The winter hemisphere experiences much stronger conversion rates, up to 10 times larger than the summer conversion rate.

The maximum magnitude of $w''b''$ in energetic regions is approximately $10^{-7} \text{ m}^2 \text{ s}^{-3}$, which is also roughly the amplitude of the seasonal cycle. In comparison, Sasaki et al. (2014, Fig. 4b) diagnosed a seasonal amplitude in baroclinic conversion of approximately $10^{-6} \text{ m}^2 \text{ s}^{-3}$ in a much higher resolution regional model of the Kuroshio. Brannigan et al. (2015, Fig. 19b) found a seasonal cycle amplitude of approximately $10^{-8} \text{ m}^2 \text{ s}^{-3}$ in an idealized model based on the mid-latitude open ocean run at 0.5 km resolution. These comparison show that the magnitude and seasonal cycle of $w''b''$ in the POP model is consistent with, but somewhat weaker than, higher resolution studies of seasonal MLI in eddy active regions.

We also compare the diagnosed $\overline{w''b''}$ with an estimate given by the MLI parametrization of Fox-Kemper et al. (2008), which is based on an Eady-type model of BCI within the mixed layer (see Section 4.2 for further discussion of this model). The parameterization assumes that APE stored in mixed layer fronts is converted to EKE at the rate

$$\overline{w'b'}^{FK} = \frac{\overline{M^4 H^2}}{|f|} \quad (2)$$

where M^4 is the squared horizontal buoyancy gradient, defined as

$$M^4 \equiv \left(\frac{\partial \bar{b}^{xy}}{\partial x} \right)^2 + \left(\frac{\partial \bar{b}^{xy}}{\partial y} \right)^2, \quad (3)$$

H is the mean mixed-layer depth, and f is the Coriolis parameter. This parameterization was designed to be applied to the mesoscale buoyancy gradients, so we first average the buoyancy field horizontally over ten grid points (roughly 1°), as indicated by the symbol \bar{b}^{xy} . We then square the gradients of this coarse-grained buoyancy field and finally take the climatological average over seasons (indicated by the overbar in Eq. (2)). Since daily-resolution of buoyancy was only available at the surface, we assume that M^4 is uniform over the mixed layer.

One caveat is that the exact magnitude of the FK-parameterized conversion rate is uncertain up to a scaling factor and the magnitude of buoyancy gradient in Eq. (2) is highly sensitive to the choice of averaging scale used to define M^4 . Here we choose a scale representative of the mesoscale fronts which drive MLI. We also focus on the magnitude of the seasonal cycle, which the scaling factor cancels out and is less sensitive to the choice of averaging scale than the absolute value of the estimated conversion rate.

The JFM and JAS values of $\overline{w'b'}^{FK}$ are shown in Fig. 9. The predicted amplitude of the seasonal cycle is $10^{-7} \text{ m}^2 \text{ s}^{-3}$, comparable to the diagnosed values. However, the spatial pattern is somewhat different; while the diagnosed $\overline{w'b'}$ has clear maxima in western boundary currents, $\overline{w'b'}^{FK}$ is distributed more evenly over the open subtropical oceans. The spatial pattern of seasonal difference, however, is more similar to that of $\overline{w'b'}$. Given the relatively coarse resolution of the POP model, and the approximate nature of the Fox-Kemper parameterization, the consistency between the two supports the notion that MLI is the driver of the seasonal variations in baroclinic conversion and EKE.

Finally, we compare $\overline{w'b'}$ with small-scale (below 30 km) EKE at monthly resolution from the three example regions in Fig. 10. The two signals are highly correlated. There is some indication that the EKE lags the conversion rate by one month. This in-phase relationship suggests that seasonal changes in $\overline{w'b'}$ equilibrate quickly and are likely balanced on a month-by-month basis by changes in dissipation and / or spectral energy transfer to larger scales.

4.2. Linear stability analysis

In the preceding section, we showed that the sub-monthly baroclinic conversion rate is indicative of seasonally varying MLI. The lack of daily output of the interior fields means that we cannot directly calculate the conversion rate in spectral space. However, Qiu et al. (2014) showed that the temporal variations in finite-amplitude baroclinic conversion were well captured by variations in the linear stability properties of the background ocean state. Here we use linear BCI analysis of the POP model climatology to investigate the temporal scales, spatial scales, and the vertical structure of potential instabilities.

We first calculate the growth rates of linear instabilities numerically using the same approach as Smith (2007). This method solves the linear quasigeostrophic (QG) eigenvalue problem using the local profile of geostrophic shear and stratification (N^2) at each point in the horizontal to define the background state. While Smith (2007) considered just the annual mean climatology, here we use a seasonally resolved climatology, revealing how instability varies between winter and summer.

The background state was defined by taking the seasonal climatology over 41 years of model output and aggregating the original 0.1° resolution to 1° . It is instructive to consider the winter and summer climatological profiles of geostrophic velocity and

N^2 , as shown in Fig. 11(a), an example from the Kuriosio region. While there are some seasonal difference in geostrophic velocity and associated shear, the dominant seasonal change is in the upper ocean N^2 , which is nearly 100 times weaker in the winter profile. This weak winter stratification reflects the cumulative impact of deeper winter mixed layers. The winter N^2 profile can be viewed as a superposition of interannual and intra-seasonal MLD variability over the averaging period. It is, however, problematic to attempt to define an actual mixed-layer depth from the climatological profile; because mixed-layer depth identification (e.g. using a density threshold criterion (de Boyer Montégut et al., 2004)) is a nonlinear operation, the average of the MLD given by the daily resolution output is not the same as the MLD of the climatological density field. For this reason, we define the ML as the depth over which N^2 experiences significant seasonality (approximately 160 m in Fig. 11(a), the depth at which N_{JFM}^2 and N_{JAS}^2 coincide). The ML corresponds roughly with the maximum winter MLD over the averaging interval.

The growth rates of the linear instabilities were determined numerically using the oceanmodes python package² developed for this study (hereon we will refer to this as the numerical solution). The numerical details of the linear stability calculation are given in Appendix A.5; here we show only the final results. The growth rates for the same Kuroshio example region are shown in Fig. 11(c) as a function of zonal wavenumber. (In the example, meridional wavenumber is set to zero, but full two-dimensional stability calculations were also performed.) This figure also shows several relevant length scales: the full-depth Rossby radius R_d , the mixed-layer (ML) Rossby radius R_d^{ML} , and the model Nyquist wavelength (defined as two grid points $2\Delta x$). R_d was calculated numerically with the oceanmodes package using the seasonal climatology of N^2 (buoyancy frequency), while R_d^{ML} was derived from the depth averaged buoyancy frequency over the mixed layer (i.e. $R_d^{ML} = \overline{N^{ML}} H_{ML} (\pi f)^{-1}$).

We observe large differences between winter and summer numerical growth rates, especially at small scales. A large portion of the small scale instability predicted cannot be resolved by the model, since it occurs at smaller scales than the model grid scale (thick black line in Fig. 11c). However, there is still a large seasonal difference in the resolved growth rates around the model Nyquist wavelength and above³. The vertical structure of the mode with a local maximum growth rate around the Nyquist wavelength, shown in Fig. 11b, is strongly surface intensified. This is the smallest instability that can potentially be resolved, although its growth is likely strongly damped by numerical dissipation.

To quantify the contribution of the reduced near-surface stratification during winter to the growth rates, we artificially homogenize the stratification during winter in the ML to the value at the base of ML and then recalculate the numerical growth rate, leaving the geostrophic velocity profiles untouched. The blue dotted line in Fig. 11c shows the growth rate (σ_{JFM}^{ML}) for this modified N^2 profile. We see that the large growth rates at small scales disappear, while the growth rates near the full-depth deformation radius remain unchanged. This experiment reveals that the main driver of seasonality in growth rates is indeed the weak near-surface stratification in winter. Furthermore, the lack of significant seasonal changes in deep shear/stratification and corresponding large-scale growth rates indicates that deep BCI is unlikely to be the main

² This open source package is available at <https://github.com/rabernat/oceanmodes>. Appendix A.5.

³ Within the ML, the background state of shear and stratification is ill-determined. This limits our interpretation of the actual values of the growth rates but our point shown below is that the large seasonal difference is due to the reduced ML stratification during winter time.

driver of seasonality. This general behavior holds for all the seven example regions (not shown).

The importance of weak upper ocean stratification in driving seasonality in instability is consistent with the MLI mechanism (Boccaletti et al., 2007; Callies et al., 2015; 2016). To test the quantitative connection to MLI theory, we compare the full growth rates to the approximated baroclinic instability models of Eady (1949) (Fig. 11c), which is considered to be a good approximation for MLI (Boccaletti et al., 2007; Callies et al., 2016). The analytical Eady growth rates were calculated using the two different assumptions for the Rossby deformation radius: full depth and ML⁴. We find that the ML Eady growth rates during winter are a good proxy for the full numerical solution in the Kuroshio region, capturing roughly the scale and magnitude of the dominant peak (although the numerical solutions contain even smaller-scale instabilities)⁵. Since the ML depth is related to the maximum winter ML depth, it is not surprising that the ML Eady and ML Rossby wavelength L_d^{ML} ($\equiv 2\pi R_d^{ML}$) capture the scales and large growth rates of this mode of instability. Examination of all seven example regions revealed that the ML Eady model qualitatively captures the dominant mode of baroclinic instability around the Nyquist wavelength during winter in eddy active regions (not shown).

We now assess the seasonality in linear instability at the global scale. In Fig. 12, we show the seasonal difference of the maximum numerical growth rates at the Nyquist wavelength (σ_N). (The maximum was taken from the two-dimensional zonal/meridional-wavenumber space.) We see that the maximum growth rates are consistently larger during winter than summer, consistent with the example region examined above and coherent with the seasonal pattern of EKE spectra. It is particularly notable that the reversal of seasonal signals in the tropics of the Pacific Ocean show up both in the EKE and growth rates. The large seasonal difference in growth rates are not just at the Nyquist wavelength but extend to larger scales, as seen in Fig. 11.

If MLI is indeed the driver of the seasonal variations seen in the KE spectra, the unstable mixed-layer modes must be resolved by the model grid. The 0.1° resolution of the POP model is very fine for a climate model, but it is still not even classified as mesoscale resolving at high latitudes (Hallberg, 2013)⁶. We argued above that the growth rate at small scales is due to MLI, with a peak at roughly the mixed layer deformation scale L_d^{ML} . The degree to which this is resolved at a particular location depends, then, on how L_d^{ML} varies with grid resolution, or Nyquist wavelength $2\Delta x$. In Fig. 11, we showed that the large growth rates around the Nyquist

⁴ Due to how the MLD was defined, ML Eady estimates have only been given for winter. The Eady growth rates were defined as

$$\sigma_{Eady} = f_0 \sqrt{\frac{1}{Ri}} \left[\left(\coth \frac{\mu}{2} - \frac{\mu}{2} \right) \left(\frac{\mu}{2} - \tanh \frac{\mu}{2} \right) \right]^{1/2}, \quad k_{max} = 1.6 R_d^{-1}$$

where

$$\sqrt{\frac{1}{Ri}} = \sqrt{\frac{1}{H} \int_{-H}^0 \frac{\left(\frac{\partial u_k}{\partial z} \right)^2 + \left(\frac{\partial v_k}{\partial z} \right)^2}{N^2} dz}$$

and H is the full depth or MLD depending on the context.

⁵ Unsurprisingly, the (full-depth) Eady solutions using R_d do not provide a very good fit to the numerical solution as it is difficult to assume that the stratification is uniform over the whole depth (Fig. 11(c)). Henceforth, we will not further consider the full-depth Eady growth rate. Eady (1949) also derived a solution for a model of weak stratification overlying a strong but finite-amplitude thermocline, which was re-examined by Callies et al. (2016) in the context of ocean MLI. This idealization is closer to the real ocean where the ML overlies the thermocline, but here we find the ML Eady model to be sufficient.

⁶ Note that Hallberg (2013) classifies a model as mesoscale resolving if it resolves the deformation radius R_d of the first internal mode with at least two grid points. The most unstable mode of the linear instability occurs at $L_d^{ML} = 2\pi R_d^{ML} \simeq 6R_d^{ML}$. This is significantly larger than R_d^{ML} itself.

wavelength are due to the instability around L_d^{ML} where the MLD is defined in the same manner as in Fig. 11. In Fig. 13, we plot the zonal average of L_d and L_d^{ML} , and the ratio of this wavelength to the model Nyquist wavelength in winter and summer. The ratio varies from near 0.1 at low latitudes to 10 at high latitudes. Note also that in Fig. 11, the growth rate increases strongly with wavenumber near the model grid scale, implying that, even if L_d^{ML} is not resolved, the fastest-growing resolved instability will still be near the grid scale.

The analysis above shows that there is a strong seasonality in baroclinic conversion rates and growth rates at the Nyquist and larger wavelengths attributable to MLI and partially resolvable by the model. To test the connection between the seasonality in the EKE spectra and MLI globally, we now examine the correlation between the seasonal amplitude in EKE at scales below 30 km and $w''b''$, the numerical growth rate at the Nyquist wavelength (σ_N) and $w''b''$, and EKE at scales below 30 km and σ_N in Fig. 14. As EKE and $w''b''$ are directly related via the energy budget, it is not surprising that they show the highest correlation ($r = 0.72$; Fig. 14a). EKE was taken at the surface (due to model output availability) while as $w''b''$ was taken as the average over the top 100 m. Also there is leakage of EKE at scales below 30 km due to nonlinear spectral transfer and dissipation (Arbic et al., 2013; 2014). Given these caveats, the correlation of 0.72 seems quite high. The correlations with the linear instability growth rates (Fig. 14b and c) are lower (0.58 for $w''b''$ and σ_N ; 0.49 for σ_N and EKE), but still positive. Processes such as nonlinear turbulent interactions and insufficient model resolution towards higher latitudes (Fig. 13) could be the cause of the lower correlation with the linear instability growth rate. Nevertheless, these correlations further support the hypothesis that the seasonality seen in Figs. 4 and 5 is due to MLI.

4.3. Timescale of EKE inverse cascade

The EKE spectra (Fig. 3) also show weak seasonal variations at larger scales. The energy in the smallest scales peaks in winter, while the energy in the larger mesoscale range (between 50 km and 100 km, i.e. $10^{-2} - 2 \times 10^{-2}$ cpkm) peaks in spring. Sasaki et al. (2014) and Qiu et al. (2014) argued that seasonality in submesoscale energy cascades upscale, with a time lag, to induce seasonality in the mesoscale. In this mechanism, during winter time, deeper ML and reduced stratification lead to enhanced MLI (Boccaletti et al., 2007; Fox-Kemper et al., 2008), which becomes an energy source during wintertime at the smallest scales. This excess energy cascades inversely and reaches the mesoscale in the springtime. The inverse cascade of geostrophic KE was shown extensively by Arbic et al. (2013; 2014) to be a robust phenomena regardless of the spatial resolution even in the presence of dissipation. To test whether this is a plausible explanation for the POP model mesoscale seasonality, we can quantify the time-lag in the inverse energy cascade via the eddy turnover timescale. The eddy turnover timescale quantifies the rate at which energy is transferred across scales via nonlinear eddy-eddy interaction. It is defined as

$$\tau_k = \frac{k^{-1}}{v_k} = [k^3 \mathcal{E}(k)]^{-1/2} \quad (4)$$

(e.g. Vallis, 2006) where k , v_k , and $\mathcal{E}(k)$ are the wavenumber, eddy velocity associated the wavenumber and the EKE spectrum respectively. τ_k can be considered as the approximate timescale of the spectral energy transfer. As shown in Fig. 15, we obtain values of 40–50 days in the mesoscale range and 100 days for regions with low eddy activity (not shown). These timescales are consistent with the mechanism in previous studies (e.g. Sasaki et al., 2014; Qiu et al., 2014) and suggest that the EKE spectra (Fig. 3) may re-

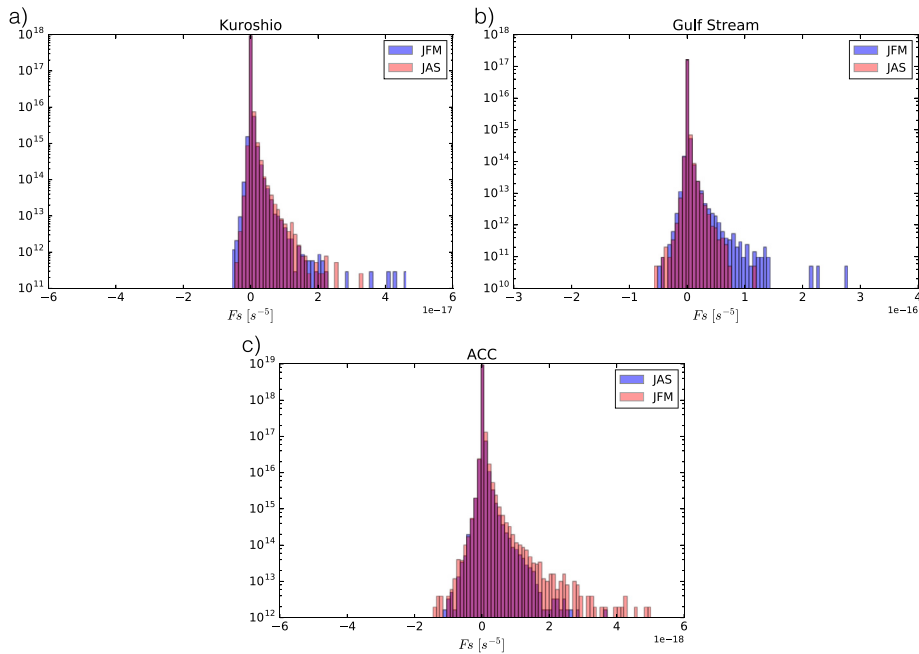


Fig. 16. Histogram of the frontogenesis function in the a) Kuroshio, b) Gulf Stream and c) ACC regions shown in Fig. 1. The y-axis is in a log scale to emphasize the seasonality and the histograms are normalized so that the area integrates to unity.

flect a time-lagged cascade of submesoscale energy to larger scales. One caveat is, however, we may be underestimating the “true” values of ε in the simulation due to the presence of dissipation, and hence overestimating τ_k . As the temporal and spatial resolution increases, less energy will be dissipated due to dissipation so we would expect the real ocean to have smaller τ_k than our estimates.

5. Other possible mechanisms for seasonality in EKE

In this section, we examine alternative possible mechanisms for the generation of seasonal variability in EKE at and below the 30 km scale.

5.1. Variation in gravity wave energy

In a recent study, Rocha et al. (2016b) attribute some seasonality in upper ocean kinetic energy to inertia-gravity waves, particularly during summer. It is important to note that the POP simulation does not include tidal forcings (Small et al., 2014), so the main mechanism for generation of super-inertial energy is high-frequency wind forcing. We quantify the contribution of the inertia-gravity waves by decomposing the horizontal kinetic energy spectra into rotational (ψ) and divergent (ϕ) components (Callies and Ferrari, 2013; Bühler et al., 2014; Rocha et al., 2016a), which assumes isotropy and homogeneity of the field. The decomposed spectra indicates the energy contained in each component (ψ, ϕ) respectively. Internal gravity waves are divergent by nature in a 2D sense, while balanced flow is non-divergent to leading order, and so the divergent spectrum approximates the kinetic energy contained in internal gravity waves.

We performed this decomposition in the same seven regions where we did the linear stability analysis. Fig. 3 (d–f) and 17 (e–h) show that for all regions, except for the highest wavenumbers, the rotational component dominates for both seasons. The seasonality seen in the POP simulation at scales larger than 50 km, therefore, is mostly due to the rotational component of the velocity field, i.e. geostrophic turbulence, which is non-divergent to first order. The divergent component at the highest wavenumbers is possibly due to small-scale dissipation producing significant ageostrophic motion.

5.2. Variation in frontogenesis

Another proposed mechanism for generating submesoscale energy is frontogenesis (FG) (Mensa et al., 2013). FG is initiated by mesoscale straining, which sharpens buoyancy fronts. Below the surface, secondary ageostrophic circulation act to flatten out the isopycnal slopes, but at the surface, the ageostrophic vertical velocities vanish and the buoyancy fronts sharpen more rapidly (Capet et al., 2008a). The resulting thermal wind shear leads to sharply surface-intensified EKE in the submesoscale range.

The relevance of strain-induced FG (McWilliams, 2016) in producing seasonality at submesoscales can be quantified via the frontogenesis function, defined as

$$F_s = \mathbf{Q}_s \cdot \nabla_z b \quad (5)$$

where ∇_z is the horizontal gradient and

$$\mathbf{Q}_s = -\left(\frac{\partial u}{\partial x} \frac{\partial b}{\partial x} + \frac{\partial v}{\partial x} \frac{\partial b}{\partial y}, \frac{\partial u}{\partial y} \frac{\partial b}{\partial x} + \frac{\partial v}{\partial y} \frac{\partial b}{\partial y} \right). \quad (6)$$

F_s represents the instantaneous rate of increase of the horizontal buoyancy gradient variance arising from the straining by the horizontal velocity field (Hoskins, 1982; Capet et al., 2008a; Brannigan et al., 2015) (as in Capet et al. (2008a) where we neglect the vertical advection term). Histograms of F_s from different seasons and regions are shown in Fig. 16. The distributions are strongly skewed toward positive values, which is expected as advective velocities act to strengthen fronts. Although there is seasonality in the Kuroshio and Gulf Stream region, it is very weak (the y-axis is in log scale). As for the ACC region, the seasonality is out of phase from that of EKE spectra (Fig. 5), i.e. EKE is higher during JAS (austral winter) but the frontogenesis function has a longer tail during JFM (austral summer). The other regions (shown in Appendix A.1) mostly show opposite seasonality from EKE, as in the ACC⁷. This is consistent with Brannigan et al. (2015), who

⁷ The EKE in the tropical Pacific domain had opposite seasonality from the rest of the domain, i.e. higher EKE during summertime, so the seasonality of F_s in the East Pacific domain is out of phase as well.

found strong FG in summer/late fall and strong symmetric instability and MLI in the winter-early spring. Since EKE at scales smaller than 30 km has highest levels during winter for both hemispheres, frontogenesis is not likely to be the cause for the EKE seasonality in the POP simulation. Although FG does not seem to be the dominant factor in causing seasonality in EKE, we did find that FG is strongest during summertime, consistent with results shown by Brannigan et al. (2015). One possible explanation is that the energetic MLI during winter counteracts FG by slumping the isopycnals, which FG feeds off of and as a result, FG is strongest during summer when MLI is weak. Since this is the time of year when the MLD is shallowest, FG may still be an important mechanism for transporting tracers across the ML base and impacting the biogeochemistry in the surface layer.

6. Conclusions

We have assessed the seasonality in ocean surface eddy kinetic energy in the ocean component of a global climate model. Although this model is not considered submesoscale-resolving, our analysis clearly shows significant seasonal differences in both magnitudes and spectral slopes of wavenumber power spectra of EKE, with a clear signature of seasonally varying mixed-layer baroclinic instability as its primary driver. This is the central result of our study.

In terms of the actual values of the spectral slopes, it was difficult to extract physical meanings and compare them to turbulent inertial range predictions because the subgrid diffusion impacted the spectra over a wide range of wavenumbers. We therefore calculated the seasonal difference of spectral slopes at scales between 200 and 250 km ($4 \times 10^{-3} - 5 \times 10^{-3}$ cpkm), while for the smallest scales (below 30 km), we simply calculated the seasonal difference in total energy and variance. Spring had the shallowest slopes and wintertime had the highest energy at the smallest scales.

As mentioned in the introduction, there have been four major hypotheses proposed in explaining seasonality in mesoscale turbulence: (i) variation in internal gravity waves due to seasonality in re-stratification of the upper ocean (Rocha et al., 2016b); (ii) variation in frontogenesis due to seasonality in lateral strain and convergence in the horizontal density gradients (Mensa et al., 2013); (iii) variation in the interior baroclinic instability (BCI) due to seasonality in the vertical shear of the full-depth background state (Qiu et al., 2014); and (iv) variation in the mixed-layer BCI (MLI) due to seasonality in ML stratification, depth and vertical shear in the mixed layer (Boccaletti et al., 2007; Qiu et al., 2014; Callies et al., 2016). We have sought to figure out which of these mechanisms, if any, are active in the POP simulation.

We found that the seasonality seen in the EKE field is consistent with observational studies and the predictions of MLI, which can be approximated by the ML Eady model in eddy-active regions (e.g. Callies and Ferrari, 2013; Callies et al., 2015). When the ML depth is deeper during wintertime, available potential energy for BCI increases. This energizes the entire mixed layer and, subsequently, the submesoscale range through non-linear interactions among scales in turbulence (Callies et al., 2015; Brannigan et al., 2015). Since the grid scale of the POP simulation is on the same order of the length scale at which the growth rate of MLI is largest, MLI is at least partially resolved in the POP simulation. Due to the inverse cascade, energy is transported between scales from small to large (Arbic et al., 2013; 2014), which is likely what is seen in the wavenumber spectra. Sasaki et al. (2014) and Qiu et al. (2014) showed a time-lag in the energy to cascade upscale, and our results are consistent with their finding; winter has the highest energy at the smallest scales, spring and autumn spectra have the highest and lowest energy respectively in the range of

50–100km ($10^{-2} - 5 \times 10^{-2}$ cpkm) and summertime has the highest energy at the largest scales.

The POP simulation has the spatial resolution of 0.1° in latitude and longitude. Due to the subgrid diffusion, however, the effective spatial resolution is much coarser. Consequently, we were very surprised to find evidence of a partially resolved seasonal cycle in MLI. Nevertheless, multiple lines of evidence support the hypothesis of MLI being the dominant cause for seasonality of small-scale EKE in this simulation. There is no such evidence for the other proposed mechanisms we considered (inertia-gravity waves, deep BCI or frontogenesis).

Although there have been numerous studies of MLI in idealized models (Boccaletti et al., 2007; Fox-Kemper et al., 2008; Fox-Kemper and Ferrari, 2008; Brannigan et al., 2015; Callies et al., 2016) and specific regions (Qiu et al., 2014; Callies et al., 2015), this is the first study describing a simulations which resolves the seasonal cycle of MLI on a global scale. It is likely that the MLI in the POP model is severely damped and consequently unrealistic in many respects. Nevertheless, the presence of clear seasonality signals at 30 km (3.3×10^{-2} cpkm) and below in every ocean basin implies a robust mechanism for seasonality despite the limited resolution of the model. The implications of this seasonality for air-sea interaction, ocean ecosystems, and eddy fluxes are important questions for future research.

Acknowledgments

This research was supported by NASA Award NNX16AJ35G. Abernathey acknowledges additional support from NSF Award OCE-1553593. Uchida acknowledges additional support from the Heiwa Nakajima Foundation. We thank Frank Bryan and Justin Small for sharing the CESM simulation outputs. Data was accessed via the Yellowstone computing system (ark:/85065/d7wd3xhc), provided by NCAR's Computational and Information Systems Laboratory, sponsored by the National Science Foundation. We also thank Jörn Callies and another anonymous reviewer for their constructive feedback.

Appendix

A.1. Isotropic wavenumber spectra and histogram of the frontogenesis function in other regions

Fig. 17 shows the isotropic wavenumber spectra of EKE and buoyancy for regions other than the ones shown in **Fig. 3** for each season. The EKE spectra is decomposed into the rotational and divergent component.

Fig. 18 shows the histogram of the frontogenesis function for winter and summertime for the same region as **Fig. 17**. We see that the PDFs are strongly skewed towards positive values and that the seasonality is opposite from that of EKE (**Fig. 5**).

A.2. Sub-monthly spectrum of EKE

We define the sub-monthly velocity anomaly as

$$\boldsymbol{v}'' = \boldsymbol{v} - \bar{\boldsymbol{v}}^m \quad (7)$$

where the superscript m represents the individual monthly mean. The sub-monthly EKE (defined as $EKE'' = 0.5(u'' + v'')$) is show in **Fig. 19** for the Kuroshio, Gulf Stream and ACC domain. Rest of the domains are shown in **Fig. 17**. We see that the monthly mean acts virtually as a low-pass spatial filter and the small-scale features are retained in the anomaly field from that.

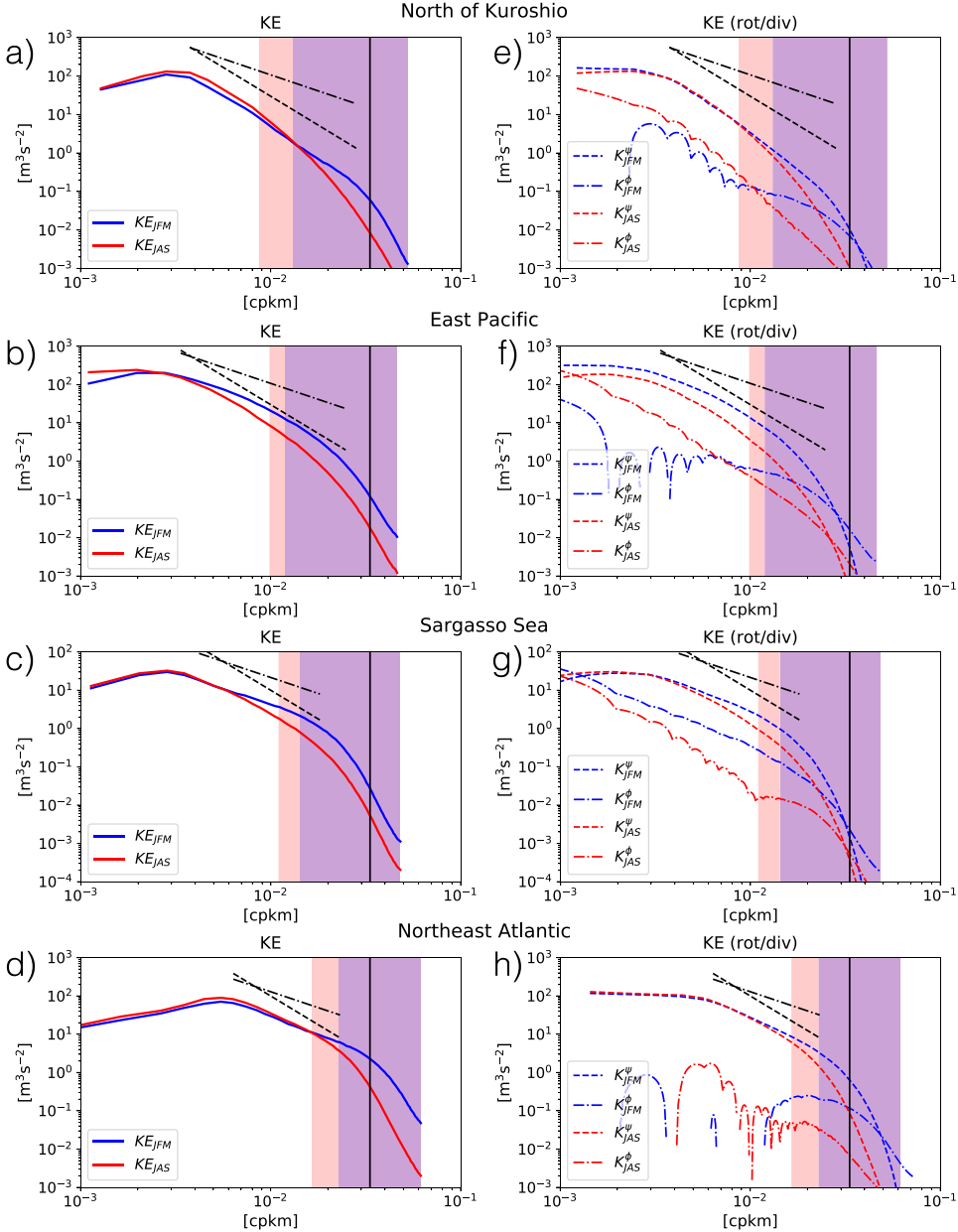


Fig. 17. Seasonally-averaged spectra in: (a) north of Kuroshio, (b) east Pacific, (c) Sargasso Sea, and (d) northeast Atlantic. The colored dotted-dashed lines show the EKE'' spectrum derived using the velocity anomaly from the monthly mean. The shading shows the dissipation range defined as where 80% of the dissipation due to biharmonic diffusion occurs and the black dashed and dotted lines show the spectral slope of -3 and -5/3 respectively. Panels (e)–(h) show the rotational and divergent component of the full EKE.

A.3. Method for calculating isotropic spectra

Here we derive the normalization factors related to the calculation of isotropic wavenumber spectra. For an arbitrary 2D scalar quantity $\theta(x, y)$ with units of $[D]$, the corresponding isotropic wavenumber spectrum is denoted as $B(k_r)$, where k_r is the isotropic wavenumber. We wish for $B(k_r)$ to satisfy the Plancherel theorem, such that that the total variance is the same when averaged over space or integrated over wavenumber, i.e.

$$\overline{\theta^2}^{xy} = \frac{1}{XY} \int_{-\infty}^{\infty} \int_{-\infty}^{\infty} \theta^2(x, y) dx dy = \int_0^{\infty} B(k_r) dk_r \quad [D^2].$$

the first integral is a spatial average, and the second is a spectral integral. X and Y are the spatial domain lengths respectively.

We now need to relate $B(k_r)$ to quantities we can calculate numerically. For a two-dimensional Fourier transform (FT), the in-

verse transform is

$$\theta(x, y) = \int_{-\infty}^{\infty} \int_{-\infty}^{\infty} \hat{\theta}(k, l) e^{2\pi i(kx+ly)} dk dl$$

where k and l are zonal and meridional wavenumber. The FT is then

$$\begin{aligned} \hat{\theta}(k, l) &= \int_{-\infty}^{\infty} \int_{-\infty}^{\infty} \theta(x, y) e^{-2\pi i(kx+ly)} dx dy \\ &\approx \Delta x \Delta y \sum_p \sum_q \theta(x_p, y_q) e^{-2\pi i(kx_p+ly_q)} \quad [D m^2] \end{aligned}$$

where the second equality represents the approximation of discretizing the continuous (FT) into a Fourier series. $\hat{\theta}$ has the units of $[D m^2]$. Numerical simulations and observations are in most cases discretely sampled data so the discrete FT is necessary. For convenience, we define another variable, indicated by a tilde, for

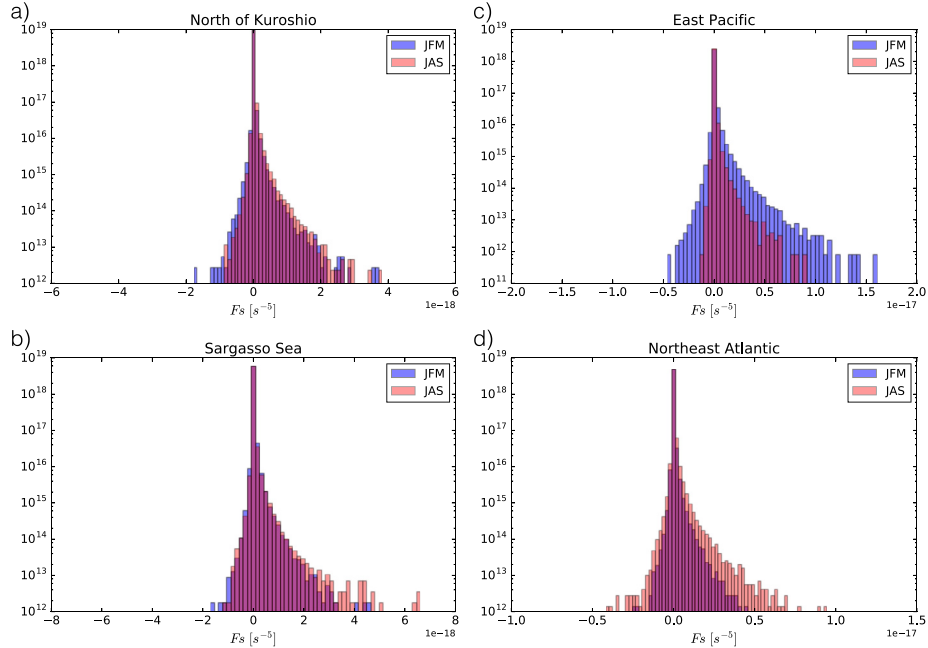


Fig. 18. Histogram of the frontogenesis function in the a) North of Kuroshio, b) Sargasso Sea, c) East Pacific and d) Northeast Atlantic regions shown in Fig. 1. The y-axis is in a log scale to emphasize the seasonality.

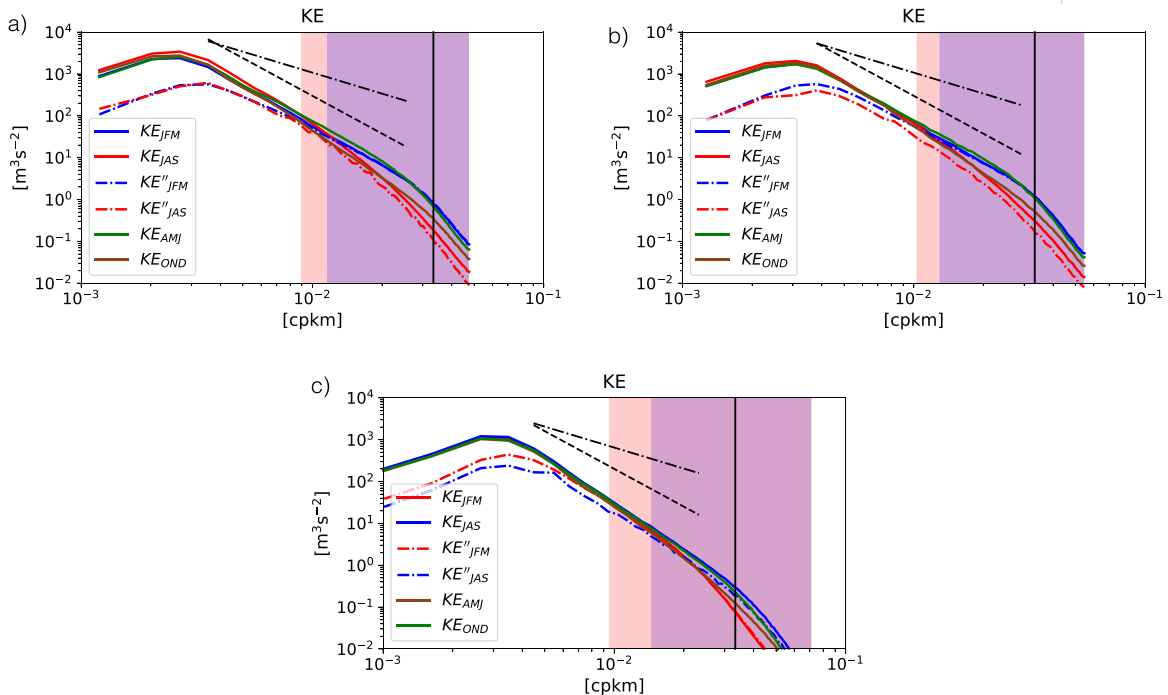


Fig. 19. Seasonally-averaged spectra in: (a) Kuroshio, (b) Gulf Stream, and (c) ACC. The colored dotted-dashed lines show the EKE'' spectrum derived using the velocity anomaly from the monthly mean. The shading shows the dissipation range defined as where 80% of the dissipation due to biharmonic diffusion occurs and the black dashed and dotted lines show the spectral slope of -3 and $-5/3$ respectively.

which we absorb the spatial units into the Fourier representation, i.e.

$$\tilde{\theta}(k, l) \equiv \sum_p \sum_q \theta(x_p, y_q) e^{-2\pi i(kx_p + ly_q)}$$

which has the units of $[D]$. The Plancherel theorem in two-dimensions (2D) is

$$\int_{-\infty}^{\infty} \int_{-\infty}^{\infty} \theta(x, y)^2 dx dy = \int_{-\infty}^{\infty} \int_{-\infty}^{\infty} |\hat{\theta}(k, l)|^2 dk dl.$$

Writing out the right-hand side (RHS) in a discrete form, we obtain

$$\begin{aligned} \Delta x \Delta y \sum_p \sum_q \theta(x_p, y_q)^2 &\approx \int_{-\infty}^{\infty} \int_{-\infty}^{\infty} \theta(x, y)^2 dx dy \\ &= \int_{-\infty}^{\infty} \int_{-\infty}^{\infty} |\hat{\theta}(k, l)|^2 dk dl \end{aligned}$$

$$\begin{aligned} &\approx \Delta k \Delta l \sum_m \sum_n |\hat{\theta}(k_m, l_n)|^2 \\ &= \Delta k \Delta l (\Delta x \Delta y)^2 \sum_m \sum_n |\tilde{\theta}(k_m, l_n)|^2. \end{aligned}$$

Δx , Δy are the spacings between the data points in the spatial domain and Δk , Δl are the spacings between each discrete inverse wavelength. The discrete inverse wavelengths are defined as

$$\begin{aligned} k &\equiv \frac{(-\frac{N_x}{2}, \dots, -1, 0, 1, \dots, \frac{N_x}{2} - 1)}{N_x \Delta x} \\ l &\equiv \frac{(-\frac{N_y}{2}, \dots, -1, 0, 1, \dots, \frac{N_y}{2} - 1)}{N_y \Delta y}, \end{aligned}$$

where N_x , N_y are the number of data points in the spatial domain.

Hence, the Plancherel relation in the discrete form becomes

$$\Delta x \Delta y \sum_p \sum_q \theta(x_p, y_q)^2 = \frac{1}{N_x^2 N_y^2 \Delta k \Delta l} \sum_m \sum_n |\tilde{\theta}(k_m, l_n)|^2.$$

Now, defining the normalized discrete Fourier coefficients as

$$\check{\theta}(k_m, l_n) \equiv \frac{1}{N_x N_y \sqrt{\Delta k \Delta l}} \tilde{\theta}(k_m, l_n) \quad [D \text{ m}] \quad (\text{A-1})$$

in which $\check{\theta}$ represents the square root of power spectral density (PSD), the discrete Plancherel theorem becomes

$$\Delta x \Delta y \sum_p \sum_q \theta(x_p, y_q)^2 = \sum_m \sum_n |\check{\theta}(k_m, l_n)|^2.$$

The isotropic PSD, however, needs to be defined carefully. Since it involves a transformation to polar coordinates, we pick up an extra factor of k_r in the integral. In order to satisfy the Plancherel's relation in 2D, we need

$$\begin{aligned} &\int_0^\infty \int_{-\pi}^\pi B(k_r, \phi) d\phi dk_r = \overline{\theta^{xy}} = \int_0^\infty \int_{-\pi}^\pi (|\hat{\theta}(k_r, \phi)|^2 k_r d\phi) dk_r \\ &\approx \frac{1}{\pi R^2} \int_0^R \left(\int_{-\pi}^\pi |\hat{\theta}(k_r, \phi)|^2 k_r d\phi \right) dk_r \quad [D^2] \\ \therefore \quad &\int_{-\pi}^\pi B_{2D}(k_r, \phi) d\phi = \frac{1}{\pi R^2} \int_{-\pi}^\pi |\hat{\theta}(k_r, \phi)|^2 k_r d\phi \quad [D^2 m] \end{aligned}$$

where $\Delta k_r \equiv \frac{1}{N_r \Delta r}$ and N_r , Δr are the number of data points in the radial direction and spacing between the data points respectively.

For an isotropic field, this reduces to

$$\begin{aligned} \overline{\theta^{xy}} &= \int_0^\infty B_{2D}(k_r) dk_r \approx \sum_n B_{2D}(k_{rn}) \Delta k_r \\ &= (\Delta k_r)^3 \sum_n \frac{k_{rn}}{\pi} |\hat{\theta}(k_{rn})|^2 \quad [D^2]. \end{aligned}$$

Using the results above, the relation between the Cartesian and polar coordinate for the Fourier components are

$$\begin{aligned} |\hat{\theta}(k_m, l_n)|^2 &= (N_x \Delta x)(N_y \Delta y) |\check{\theta}(k_m, l_n)|^2 \Leftrightarrow |\hat{\theta}(k_{rn}, \phi)|^2 \\ &= \pi (N_r \Delta r)^2 |\check{\theta}(k_{rn}, \phi)|^2 \Leftrightarrow |\hat{\theta}(k_{rn}, \phi)|^2 \\ &= \frac{\pi}{(\Delta k_r)^2} |\check{\theta}(k_{rn}, \phi)|^2 \quad [D^2]. \end{aligned}$$

In an isotropic state

$$|\hat{\theta}(k_{rn})|^2 = \frac{\pi}{(\Delta k_r)^2} |\check{\theta}(k_{rn})|^2 \quad [D^2].$$

Hence the PSD $B_{2D}(k_r)$ becomes

$$B_{2D}(k_{rn}) = k_{rn} \frac{(\Delta k_r)^2}{\pi} |\hat{\theta}(k_{rn})|^2 = k_{rn} |\check{\theta}(k_{rn})|^2 \quad [D^2 m].$$

A.4. Confidence interval for spectra

We shall refer to Menke and Menke (2009). From the Plancherel theorem, we have

$$\begin{aligned} &\Delta x \Delta y \sum_{p=0}^{N_x-1} \sum_{q=0}^{N_y-1} w^i(x_p, y_q) d^i(x_p, y_q) \\ &\approx \iint [w(x, y) d(x, y)]^2 dx dy \\ &= \iint |d^i(k, l)|^2 dk dl \\ &\approx \Delta k \Delta l \sum_{m=-N_x/2+1}^{N_x/2} \sum_{n=-N_y/2+1}^{N_y/2} |\hat{d}^i(k_m, l_n)|^2 \end{aligned}$$

where $w(x, y)$ and $d(x, y)$ are the tapering function and data respectively and \hat{d} includes the tapering. Using the relation shown in the Appendix A.3 yields

$$\begin{aligned} &\Delta k \Delta l \sum_m \sum_n |\hat{d}^i(k_m, l_n)|^2 \\ &= \Delta k \Delta l (\Delta x \Delta y)^2 \sum_{m=-N_x/2+1}^{N_x/2} \sum_{n=-N_y/2+1}^{N_y/2} |\tilde{d}^i(k_m, l_n)|^2 \end{aligned}$$

so we get

$$\begin{aligned} &\sum_p \sum_q (w^i(x_p, y_q) d^i(x_p, y_q))^2 \\ &= \frac{1}{N_x N_y} \sum_{m=-N_x/2+1}^{N_x/2} \sum_{n=-N_y/2+1}^{N_y/2} |\tilde{d}^i(k_m, l_n)|^2 \quad (*). \end{aligned}$$

We can approximate the left-hand side (LHS) of the equation above as

$$\begin{aligned} (N_x N_y) \sum_p \sum_q (w^i(x_p, y_q) d^i(x_p, y_q))^2 &\sim \sum_p \sum_q w_{pq}^i {}^2 \sum_p \sum_q d_{pq}^i {}^2 \\ &= \frac{1}{N_x N_y} \sum_p \sum_q w_{pq}^i {}^2 (N_x N_y)^2 \frac{1}{N_x N_y} \sum_p \sum_q d_{pq}^i {}^2 = (N_x N_y)^2 f_T f_d \end{aligned}$$

where " ~ " means equivalent in a statistical sense and we have defined $f_T \equiv \frac{1}{N_x N_y} \sum_p^N \sum_q^N (w_{pq}^i)^2$, $f_d \equiv \frac{1}{N_x N_y} \sum_p^N \sum_q^N (d_{pq}^i)^2$. When no tapering is applied, the right-hand side (RHS) above becomes $(N_x N_y)^2 f_d$. The Plancherel relation (*) above becomes

$$f_T f_d \simeq \frac{1}{(N_x N_y)^2} \sum_{m=-N_x/2+1}^{N_x/2} \sum_{n=-N_y/2+1}^{N_y/2} |\tilde{d}^i(k_m, l_n)|^2 = \frac{1}{N_x N_y} \overline{|\tilde{d}^i|^2}.$$

Since the mean of a χ^2 distribution is equivalent to the number of elements summed and the variance is twice the mean, we have $\phi^i/c = 2$ or 1 and $\sigma_{\phi^i}^2/c^2 = 4$ or 2 where $\phi^i \equiv |\tilde{d}^i|^2$ and c is the normalization factor. Thus,

$$c = \frac{N_x N_y f_T f_d}{2} \quad (2 \leq i \leq N/2)$$

$$c = N_x N_y f_T f_d \quad (i = 1, N/2 + 1)$$

so $\phi^i/c (\equiv \Phi)$ follows the χ^2 distribution. Since, $\Phi(k_r)$ are normalized to the χ^2 distribution, the probability that the estimated spectrum $\Phi^{est}(k_{rn})$ should be close to the true spectrum $\Phi^{true}(k_{rn})$ is:

$$p\left(\frac{2\nu\Phi^{est}(k_{rn})}{b} \leq \Phi^{true}(k_{rn}) \leq \frac{2\nu\Phi^{est}(k_{rn})}{a}\right) = 1 - \alpha$$

(Gille et al., 2015) where $1 - \alpha$ is the confidence level (i.e. $\alpha = 0.05$ for 95% confidence). a and b are the $(1 - \alpha)/2$ and $\alpha/2$ critical values of the $\chi^2(2\nu)$ distribution and ν ($= NM(r)$) is the number of chunks that are added up. The $p\%$ confidence range therefore is:

$$\frac{2\nu}{b} \leq \frac{\Phi^{true}(k_{r_m})}{\Phi^{est}(k_{r_m})} \leq \frac{2\nu}{a}.$$

Thus

$$\begin{aligned} \log(\Phi^{est}(k_{r_m})) + \log\left(\frac{2\nu}{b}\right) &\leq \log(\Phi^{true}(k_{r_m})) \\ &\leq \log(\Phi^{est}(k_{r_m})) + \log\left(\frac{2\nu}{a}\right) \end{aligned}$$

so the confidence interval is:

$$error_{high} = \log\left(\frac{2\nu}{a}\right), \quad error_{low} = \log\left(\frac{2\nu}{b}\right)$$

and to move the error bar around in the log-log dimension, we can multiply the values inside the logarithm by an arbitrary factor A .

A.5. Dissipation range

The biharmonic momentum dissipation terms are calculated as defined in the POP simulation,

$$D_H(u) = \nabla^2(A_M \nabla^2 u)$$

where

$$\begin{aligned} \nabla^2 u = & \Delta_x \delta_x \frac{\Delta_y \delta_x u}{UAREA} + \Delta_y \delta_y \frac{\Delta_x \delta_y u}{UAREA} \\ & - u [\delta_x k_x - \delta_y k_y + 2(k_x^2 + k_y^2)] + 2k_y \delta_x v - 2k_x \delta_y v. \end{aligned}$$

The coefficients k_x and k_y are the metric terms which arise when converting Cartesian coordinates to spherical coordinates. For further details of the definition of each variable, refer to Smith et al. (2010). We define the dissipation range the wavenumber above which 80% of the KE dissipation occurs, i.e.

$$0.8 = \frac{\int_{K_{diss}}^{K_{Ny}} [\tilde{u} D_H(u) + \tilde{v} D_H(v)] dK}{\int_{K_{min}}^{K_{Ny}} [\tilde{u} D_H(u) + \tilde{v} D_H(v)] dK}$$

where K_{Ny} , K_{min} , and K_{diss} are the Nyquist wavenumber, minimum wavenumber defined by the domain and the wavenumber which defines the dissipation range respectively. The $(\tilde{\cdot})$ indicates the Fourier transforms defined in Eq. (A-1).

A.6. Linear stability calculation

The oceanmodes package solves the inviscid QG equations linearized around the mean background state ($u_g = -\frac{\partial \Psi}{\partial y}$, $v_g = \frac{\partial \Psi}{\partial x}$, N^2 , Q):

$$\frac{\partial q}{\partial t} + \mathbf{u}_g \cdot \nabla q + \mathbf{u} \cdot \nabla Q = 0$$

with the boundary condition of

$$\frac{\partial b}{\partial t} + \mathbf{u}_g \cdot \nabla b + \mathbf{u} \cdot \nabla (B + N^2 \eta) = 0$$

where a plane-wave solution for the perturbation, i.e. $\psi = Re[\Phi(z)e^{i(kx+ly-\omega t)}]$ is assumed and η is the topographic slope. The velocity field is divided into the geostrophic and perturbation component. The geostrophic velocity \mathbf{u}_g is derived as

$$\mathbf{u}_g = \frac{g}{f \rho_{ref}} [\bar{\rho} \mathbf{e}_z \times \nabla \eta + (\eta - z) \mathbf{e}_z \times \nabla \bar{\rho}]$$

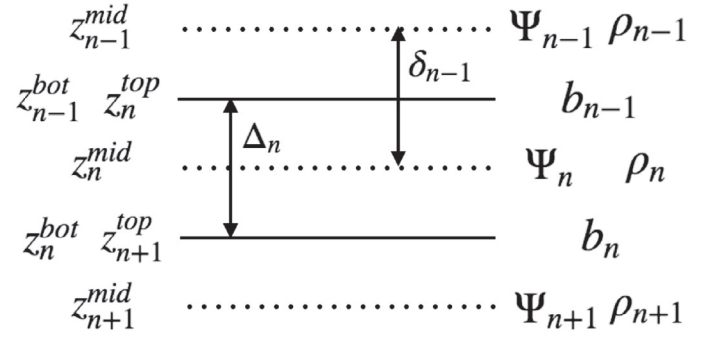


Fig. 20. The vertical layer setup of the POP model. The stream function (Ψ) and density (ρ) are defined at the midpoint of each vertical layer and buoyancy (b , N) is defined on the boundaries of each layer.

where $\bar{\rho} = \int_{-H}^0 \rho(z) dz$ and \mathbf{e}_z is the unit vector along the vertical axis. The reference density (ρ_{ref}) is taken to be the potential density at the surface.

$$q = \nabla^2 \psi + \Gamma \psi, \quad Q = \beta y + \Gamma \Psi$$

$$b = f \frac{\partial \psi}{\partial z}, \quad B = f \frac{\partial \Psi}{\partial z} \quad (= \int N^2(z) dz)$$

are the perturbed and mean QG potential vorticity (QGPV) and buoyancy respectively where $\Gamma = \frac{\partial}{\partial z} \left(\frac{f^2}{N^2} \frac{\partial}{\partial z} \right)$. The buoyancy frequency (N^2) was derived using the gsw Python package (<https://github.com/TEOS-10/python-gsw> (McDougall and Barker, 2011)).

Starting from the linearized QG potential vorticity equation around a state of rest ($\mathbf{u}_g = 0$) and prescribing a solution as $\Psi = Re[e^{i(kx+ly-\sigma t)}] \Phi(z)$, we get:

$$\begin{aligned} 0 &= \frac{\partial}{\partial t} \left[\nabla_z^2 \Psi + \frac{\partial}{\partial z} \left(\frac{f^2}{N^2} \frac{\partial \Psi}{\partial z} \right) \right] + \beta \frac{\partial \Psi}{\partial x} \\ &= i\sigma \left[(k^2 + l^2) e^{i(kx+ly-\sigma t)} \Phi - e^{i(kx+ly-\sigma t)} \frac{d}{dz} \left(\frac{f^2}{N^2} \frac{d\Phi}{dz} \right) \right] \\ &\quad + ike^{i(kx+ly-\sigma t)} \beta \Phi \\ \Gamma \Phi &\equiv \frac{d}{dz} \left(\frac{f^2}{N^2} \frac{d\Phi}{dz} \right) = -\left(k^2 + l^2 + \frac{k}{\sigma} \beta \right) \Phi \equiv -K^2 \Phi \end{aligned} \quad (\text{A-2})$$

where K is defined as 2π over wavelength, which is often referred as "Rossby deformation wavenumber". Assuming the same conditions as in Smith (2007) and taking caution of the vertical layer setup in the POP model (Fig. 20), we can discretize the equation above as:

$$\begin{aligned} \Gamma_n^m \Phi_n &= \frac{f^2}{\delta_n} \left(\frac{1}{N_n^2} \frac{\Phi_{n+1} - \Phi_n}{\Delta_n} - \frac{1}{N_{n-1}^2} \frac{\Phi_n - \Phi_{n-1}}{\Delta_{n-1}} \right) \quad (1 < n < \nu) \\ \Gamma_1^m \Phi_1 &= \frac{f^2}{\delta_1} \left(\frac{1}{N_1^2} \frac{\Phi_2 - \Phi_1}{\Delta_1} \right) \\ \Gamma_\nu^m \Phi_\nu &= \frac{f^2}{\delta_\nu} \left(\frac{-1}{N_{\nu-1}^2} \frac{\Phi_\nu - \Phi_{\nu-1}}{\Delta_{\nu-1}} \right) \end{aligned}$$

where the superscript m and subscript n ($= 1, 2, \dots, \nu$) represent the eigenmodes and vertical layer respectively.

References

- Arbic, B.K., Müller, M., Richman, J.G., Shriver, J.F., Morten, A.J., Scott, R.B., Sérasin, G., Penduff, T., 2014. Geostrophic turbulence in the frequency-wavenumber domain: eddy-driven low-frequency variability*. J. Phys. Oceanogr. 44 (8), 2050–2069.

- Arbic, B.K., Polzin, K.L., Scott, R.B., Richman, J.G., Shriver, J.F., 2013. On eddy viscosity, energy cascades, and the horizontal resolution of gridded satellite altimeter products. *J. Phys. Oceanogr.* 43 (2), 283–300.
- Blumen, W., 1978. Uniform potential vorticity flow: part i. theory of wave interactions and two-dimensional turbulence. *J. Atmos. Sci.* 35 (5), 774–783.
- Boccaletti, G., Ferrari, R., Fox-Kemper, B., 2007. Mixed layer instabilities and restratification. *J. Phys. Oceanogr.* 37 (9), 2228–2250.
- de Boyer Montégut, C., Madec, G., Fischer, A.S., Lazar, A., Iudicone, D., 2004. Mixed layer depth over the global ocean: an examination of profile data and a profile-based climatology. *J. Geophys. Res.: Oceans* 109 (C12), C12003.
- Brannigan, L., Marshall, D., Naveira-Garabato, A., Nurser, A., 2015. The seasonal cycle of submesoscale flows. *Ocean Modell.* 69–84.
- Buckingham, C.E., Naveira Garabato, A.C., Thompson, A.F., Brannigan, L., Lazar, A., Marshall, D.P., George Nurser, A., Damerell, G., Heywood, K.J., Belcher, S.E., 2016. Seasonality of submesoscale flows in the ocean surface boundary layer. *Geophys. Res. Lett.* 43 (5), 2118–2126.
- Bühler, O., Callies, J., Ferrari, R., 2014. Wave-vortex decomposition of one-dimensional ship-track data. *J. Fluid Mech.* 756, 1007.
- Callies, J., Ferrari, R., 2013. Interpreting energy and tracer spectra of upper-ocean turbulence in the submesoscale range (1–200 km). *J. Phys. Oceanogr.* 43 (11), 2456–2474.
- Callies, J., Ferrari, R., Klymak, J., Gula, J., 2015. Seasonality in submesoscale turbulence. *Nat. Commun.* 6, 1–8.
- Callies, J., Flierl, G., Ferrari, R., Fox-Kemper, B., 2016. The role of mixed-layer instabilities in submesoscale turbulence. *J. Fluid Mech.* 788, 5–41.
- Capet, X., McWilliams, J., Molemaker, M., Shchepetkin, A., 2008. Mesoscale to submesoscale transition in the california current system. part ii: frontal processes. *J. Phys. Oceanogr.* 38 (1), 44–64.
- Capet, X., McWilliams, J.C., Molemaker, M.J., Shchepetkin, A.F., 2008. Mesoscale to submesoscale transition in the california current system. part iii: energy balance and flux. *J. Phys. Oceanogr.* 38 (10), 2256–2269.
- Charney, J., 1971. Geostrophic turbulence. *J. Atmos. Sci.* 28 (6), 1087–1095.
- Chen, R., Thompson, A.F., Flierl, G.R., 2016. Time-dependent eddy-mean energy diagrams and their application to the ocean. *J. Phys. Oceanogr.* 46 (9), 2827–2850.
- Dufau, C., Orsztynowicz, M., Dibarboure, G., Morrow, R., Le Traon, P.-Y., 2016. Mesoscale resolution capability of altimetry: present and future. *J. Geophys. Res.: Oceans* 121 (7), 4910–4927.
- Eady, E.T., 1949. Long waves and cyclone waves. *Tellus* 1 (3), 33–52.
- Fox-Kemper, B., Ferrari, R., 2008. Parameterization of mixed layer eddies. part ii: prognosis and impact. *J. Phys. Oceanogr.* 38 (6), 1166–1179.
- Fox-Kemper, B., Ferrari, R., Hallberg, R., 2008. Parameterization of mixed layer eddies. part i: theory and diagnosis. *J. Phys. Oceanogr.* 38 (6), 1145–1165.
- Fu, L.-L., Ferrari, R., 2008. Observing oceanic submesoscale processes from space. *EOS* 89, 488. (Washington. DC).
- Gill, A., Green, J., Simmons, A., 1974. Energy partition in the large-scale ocean circulation and the production of mid-ocean eddies. In: Deep Sea Research and Oceanographic Abstracts, 21. Elsevier, pp. 499–528.
- Gille, S., 2015. Spectral uncertainties. <http://www-pord.ucsd.edu/~sgille/sio221c/lectures/spectra.pdf>.
- Griffies, S.M., Winton, M., Anderson, W.G., Benson, R., Delworth, T.L., Dufour, C.O., Dunne, J.P., Goddard, P., Morrison, A.K., Rosati, A., Wittenberg, A.T., Yin, J., Zhang, R., 2015. Impacts on ocean heat from transient mesoscale eddies in a hierarchy of climate models. *J. Clim.* 28 (3), 952–977.
- Gula, J., Molemaker, M.J., McWilliams, J.C., 2014. Submesoscale cold filaments in the gulf stream. *J. Phys. Oceanogr.* 44 (10), 2617–2643.
- Hallberg, R., 2013. Using a resolution function to regulate parameterizations of oceanic mesoscale eddy effects. *Ocean Modell.* 72, 92–103.
- Held, I., Pierrehumbert, R., Garner, S., Swanson, K., 1995. Surface quasi-geostrophic dynamics. *J. Fluid Mech.* 282, 1–20.
- Holland, W.R., 1978. The role of mesoscale eddies in the general circulation of the ocean-numerical experiments using a wind-driven quasi-geostrophic model. *J. Phys. Oceanogr.* 8 (3), 363–392.
- Hoskins, B., 1982. The mathematical theory of frontogenesis. *Annu. Rev. Fluid Mech.* 14 (1), 131–151.
- Jayne, S., Marotzke, J., 2002. The oceanic eddy heat transport*. *J. Phys. Oceanogr.* 32 (12), 3328–3345.
- Lapeyre, G., Klein, P., 2006. Dynamics of the upper oceanic layers in terms of surface quasigeostrophy theory. *J. Phys. Oceanogr.* 36 (2), 165–176.
- Large, W., McWilliams, J., Doney, S., et al., 1994. Oceanic vertical mixing: a review and a model with a nonlocal boundary layer parameterization. *Rev. Geophys.* 32 (4), 363–404.
- Lévy, M., Klein, P., Tréguier, A., Iovino, D., Madec, G., Masson, S., Takahashi, K., 2010. Modifications of gyre circulation by sub-mesoscale physics. *Ocean Modell.* 34 (1), 1–15.
- McClean, J., Bader, D., Bryan, F., Maltrud, M., Dennis, J., Mirin, A., Jones, P., Kim, Y., Ivanova, D., Vertenstein, M., Boyle, J., Jacob, R., Norton, N., Craig, A., Worley, P., 2011. A prototype two-decade fully coupled fine-resolution CCSM simulation. *Ocean Modell.* 39, 10–30.
- McDougall, T., Barker, P., 2011. Getting started with teos-10 and the gibbs seawater (gsw) oceanographic toolbox. In: SCOR/IAPSO WG, 127, pp. 1–28.
- McWilliams, J.C., 2016. Submesoscale currents in the ocean. *Proc. R. Soc. A* 472, 20160117.
- Menke, W., Menke, J., 2009. Environmental Data Analysis with MATLAB. Elsevier.
- Mensa, J., Garraffo, Z., Griffa, A., Özgökmen, T., Haza, A., Veneziani, M., 2013. Seasonality of the submesoscale dynamics in the gulf stream region. *Ocean Dyn.* 63 (8), 923–941.
- Qiu, B., Chen, S., Klein, P., Sasaki, H., Sasai, Y., 2014. Seasonal mesoscale and submesoscale eddy variability along the north pacific subtropical countercurrent. *J. Phys. Oceanogr.* 44 (12), 3079–3098.
- Rhines, P.B., 1979. Geostrophic turbulence. *Annu. Rev. Fluid Mech.* 11 (1), 401–441.
- Rocha, C.B., Chereskin, T.K., Gille, S.T., Menemenlis, D., 2016a. Mesoscale to submesoscale wavenumber spectra in drake passage. *J. Phys. Oceanogr.* 46 (2), 601–620.
- Rocha, C.B., Chereskin, T.K., Gille, S.T., Menemenlis, D., 2016b. Seasonality of submesoscale dynamics in the kuroshio extension. *Geophys. Res. Lett.* 11304–11311.
- Sasaki, H., Klein, P., Qiu, B., Sasai, Y., 2014. Impact of oceanic-scale interactions on the seasonal modulation of ocean dynamics by the atmosphere. *Nat. Commun.* 5, 5636.
- Schloesser, F., Cornillon, P., Donohue, K., Boussidi, B., Iskin, E., 2016. Evaluation of thermosalinograph and viirs data for the characterization of near-surface temperature fields. *J. Atmos. Oceanic Technol.* 33 (9), 1843–1858.
- Small, R., Bacmeister, J., Bailey, D., Baker, A., Bishop, S., Bryan, F., Caron, J., Dennis, J., Gent, P., Hsu, H., et al., 2014. A new synoptic scale resolving global climate simulation using the community earth system model. *J. Adv. Model. Earth Syst.* 6 (4), 1065–1094.
- Smith, R., Jones, P., Briegble, B., Bryan, F., Danabasoglu, G., Dennis, J., Dukowicz, J., Eden, C., Fox-Kemper, B., Gent, P., Hecht, M., Jayne, S., Jochum, M., Large, W., Lindsay, K., Maltrud, M., Norton, N., Peacock, S., Vertenstein, M., Yeager, S., 2010. The parallel ocean program reference manual.
- Smith, S., 2007. The geography of linear baroclinic instability in earth's oceans. *J. Mar. Res.* 65 (5), 655–683.
- Stammer, D., 1997. Global characteristics of ocean variability estimated from regional topex/poseidon altimeter measurements. *J. Phys. Oceanogr.* 27 (8), 1743–1769.
- Thomas, L., Tandon, A., Mahadevan, A., 2008. Submesoscale processes and dynamics. *Ocean Modeling in an Eddying Regime. Geophys. Monogr. Ser.* 177, 17–38.
- Vallis, G.K., 2006. Atmospheric and Oceanic Fluid Dynamics: Fundamentals and Large-scale Circulation. Cambridge University Press.
- Volkov, D., Lee, T., Fu, L., 2008. Eddy-induced meridional heat transport in the ocean. *Geophys. Res. Lett.* 35 (20).
- Xu, Y., Fu, L., 2011. Global variability of the wavenumber spectrum of oceanic mesoscale turbulence. *J. Phys. Oceanogr.* 41 (4), 802–809.
- Xu, Y., Fu, L., 2012. The effects of altimeter instrument noise on the estimation of the wavenumber spectrum of sea surface height. *J. Phys. Oceanogr.* 42 (12), 2229–2233.